involving members of the 1^- meson nonet of some as yet undiscovered heavy multiplet of baryons or mesons.

ACKNOWLEDGMENTS

We should like to thank Dr. Marcos Moshinsky for enabling us to enjoy the hospitality and stimulation of the Latin American School of Physics in Mexico City, during the summer of 1965, when much of this work was done. One of us (A. J. Macfarlane) would like to thank Dr. Jack Leitner, and the other (R. H. Socolow) would like to thank Dr. Janos Kirz and Dr. Gino Segrè for helpful discussions.

PHYSICAL REVIEW VOLUME 144, NUMBER 4 29 APRIL 1966

Wide-Angle Electron-Pair Production*†

R. B. Blumenthal, D. C. Ehn, W. L. Faissler, P. M. Joseph, L. J. Lanzerotti,‡
F. M. Pipkin, and D. G. Stairs§
Harvard University, Cambridge, Massachusetts

(Received 6 October 1965; revised manuscript received 19 January 1966)

An experiment testing quantum electrodynamics at high energies and small distances is described. The photoproduction from carbon of electron-positron pairs was measured at laboratory angles of 4.60°, 6.23°, and 7.46°. Symmetrical electron-positron pairs in the energy range from 1 to 5 BeV were detected with a magnet-counter system which consisted of two mirror-image arms. Extensive internal checks of the apparatus were made and the results were reproducible. The theoretical values for the electron-pair yield were calculated by integrating the differential pair-production cross section over the acceptance of the apparatus using a Monte Carlo technique. The ratio R= (experimental yield)/(theoretical yield) was not 1.0. R was approximately given by

$$R=0.62\{(1.00\pm0.05)+k^2/(4.31\pm0.17)^2\},$$

where k is the energy in BeV of the photon which produced the pair, and by

$$R=0.67\{(1.00\pm0.04)-Q_f^2/(313\pm13)^2\},$$

where Q_f^2 is the four-momentum of the virtual fermion in $(\mathrm{MeV})^2$. The apparatus studies and a comparison of the measured single-electron yields with the theoretical yields suggest that an error exists in the absolute normalization of the results. There are no indications that the observed variation of the electron-pair yields with momentum or the large excess of wide-angle electron pairs at high energies is due to any systematic error. The experimental results do not agree with the predictions of quantum electrodynamics; they indicate a breakdown of the theory or the presence of other processes.

I. INTRODUCTION

QUANTUM electrodynamics is one of the most firmly established theories of modern physics. This theory describes the electromagnetic interactions of electrons, muons, and photons, and, as far as is known, it also describes correctly the structure of the electron and the muon. The best evidence for the correctness of this theory comes from high-precision measurements of the energy levels of simple atoms and of the anomalous magnetic moments of the electron and muon. However, these measurements are relatively insensitive to the behavior of the theory at very small distances and high momentum transfers. It is conceivable that the theory correctly describes low-energy phenomena such as the Lamb shift and the anomalous moment of the electron but fails to describe correctly the structure of the electron or electron-electron scattering at high momentum transfers. It is also not clear whether the present theory of quantum electrodynamics (QED) arrived at by a renormalization procedure is a final theory or whether it is a temporary solution to a more involved problem. For these reasons, it is important to look for deviations from quantum electrodynamics in situations where the experiments are sensitive to the behavior of the theory at high momentum transfers or small distances.

This paper reports an experiment performed to study the behavior of the electron propagator for large space-like virtual momenta. This experiment studies the photoproduction of electron-positron pairs at large angles, and was first proposed by Drell as a technique for studying the behavior of quantum electrodynamics at small distances.[1] In the first part of the paper, the theory of the experiment is discussed; later sections describe the apparatus, the mode of analysis, and the results.

* Research supported by the U. S. Atomic Energy Commission under Contract No. AT(30-1)2752.

† This paper is based in part on material submitted by one of the authors (R. B. Blumenthal) to Harvard University in partial fulfillment of the requirements for the Doctor of Philosophy degree.

‡ Present address: Bell Telephone Laboratories, Murray Hill, New Jersey.

§ Present address: McGill University, Montreal, Canada.

[1] S. D. Drell, Ann. Phys. 4, 75 (1958).

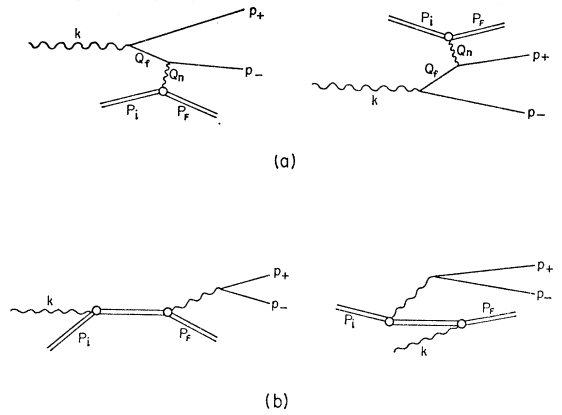

FIG. 1. Feynman diagrams for electrodynamic processes which give rise to wide-angle electron pairs. (a) The Bethe-Heitler diagrams for electron pair production. (b) The Compton diagrams considered by Bjorken, Drell, and Frautschi.

II. THEORY

The Feynman diagrams for Bethe-Heitler pair production are pictured in Fig. 1(a). The symbols used in this paper are defined in Table I and the laboratory angles are illustrated in Fig. 2.[2] The object of the experiment which tests QED is to make Q_f, the four-momentum of the virtual lepton, as large as possible. Two Feynman diagrams which are not interesting from the standpoint of testing quantum electrodynamics, but which can give electron pairs, are the Compton diagrams shown in Fig. 1(b). The contribution of the purely electromagnetic Compton processes is very small. Above the meson threshold, the contribution of the Compton-like processes can only be estimated since the meson effects are not known. For either Bethe-Heitler or Compton pair production there is complete symmetry between p_+ and p_-. However, the interference term between the Bethe-Heitler and Compton matrix elements is antisymmetric under the interchange of p_+ and p_-. Thus, if the experimental conditions are completely symmetric in p_+ and p_-, the interference term vanishes. This statement is true even for finite energy and angle acceptances if the acceptances are symmetric in p_+ and p_- or if the data is taken by spending half of the time using a given detector for electrons and the other half using that detector for positrons.

The observation of symmetrical pairs minimizes the four-momentum transferred to the carbon nucleus and thus reduces the corrections due to nuclear form factors. The interaction with the nucleus is a strong interaction, and these effects must be separated from the electrodynamics. The diagrams of Fig. 1 assume that the nuclear interaction is elastic. More generally, one should consider the diagram of Fig. 3. Drell and Walecka have investigated this problem extensively and they have shown that the nuclear interaction in pair production can be described by the same form factors that are measured in elastic and inelastic electron or muon scattering experiments.[3] Thus one can use the form factors measured in separate scattering experiments to calculate the pair-production cross section. At present, only the elastic charge form factor is well known for carbon; estimates of the inelastic form factors indicate that they should contribute less than 10% to the pair-production cross section for the momentum transfers in this experiment. Alternatively, if one assumes that inelastic processes are negligible, only the elastic charge form factor appears in the pair cross section for a spin-zero target such as carbon. Then electrodynamic effects can be isolated from nuclear-structure complications by measuring the pair cross section at angles and energies so chosen that the momentum transfer to the nucleus is constant while the momentum of the virtual fermion varies.

The electron pair-production cross section was first calculated by Bethe and Heitler.[4] They considered only

TABLE I. Symbols and their definitions.

k	four-momentum of incident photon
$k_{\max}$	maximum photon energy of the bremsstrahlung beam
P_i	four-momentum of initial nucleus
P_f	four-momentum of recoil nucleus
p_+	four-momentum of outgoing positron
p_-	four-momentum of outgoing electron
Q_f	four-momentum of the virtual fermion
Q_n	four-momentum transferred to the nucleus
Q_M	effective mass of the electron-positron final state
θ_+	angle between $\mathbf{p}_+$ and $\mathbf{k}$
θ_-	angle between $\mathbf{p}_-$ and $\mathbf{k}$
ϕ	angle between the $\mathbf{p}_+$-$\mathbf{k}$ plane and the $\mathbf{p}_-$-$\mathbf{k}$ plane
$\phi=0$	for the symmetric case
$\theta=\theta_+=\theta_-$	for the symmetric case
$E=E_+=E_-=k/2$	for the symmetric case
F_1,F_2; G_E,G_M	nuclear form factors
m	mass of the electron
M	mass of the nucleus
μ	anomalous magnetic moment of the nucleus
Z	atomic number of the nucleus
α	fine-structure constant

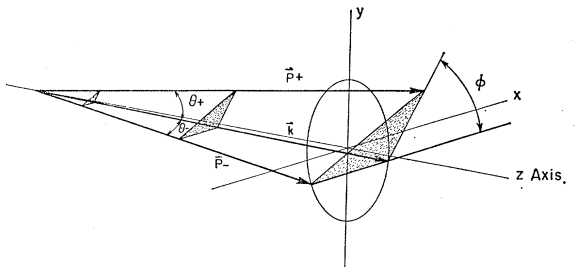

FIG. 2. Diagram showing the laboratory angles θ_+, θ_-, and ϕ.

[2] The following notation will be used: four-vectors are written as a or $(a_0,\mathbf{a})$. For momenta p the convention $p_0=E$ will also be used. The scalar product is defined as $a\cdot b=a_0b_0-\mathbf{a}\cdot\mathbf{b}$. All variables are given in the laboratory system and the choice $\hbar=c=1$ is made.

[3] S. D. Drell and J. D. Walecka, Ann. Phys. (N. Y.) **28**, 18 (1964); this reference is referred to as DW.

[4] H. Bethe and W. Heitler, Proc. Roy. Soc. (London) **146**, 83 (1934).

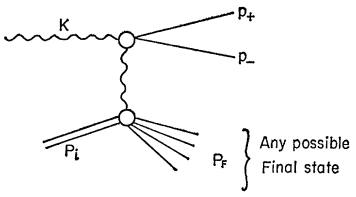

FIG. 3. Generalized diagram for Bethe-Heitler pair production.

the two diagrams of Fig. 1(a) and they neglected nuclear recoil and the nuclear form factors. Bjorken, Drell, and Frautschi (BDF) made a calculation of the cross section which included the nuclear recoil to order Q_n^3/M^3 and nuclear elastic form-factor corrections to the Bethe-Heitler formula.[5] BDF also evaluated the contribution of the Compton diagrams and the leading order radiative corrections. Drell and Walecka extended this work and arrived at an expression for the lepton pair-production cross section which includes the lepton mass and the effects of inelastic as well as elastic form factors.[3]

BDF showed that the laboratory cross section for incident photon spectrum $S(k)$ is

$$\frac{d\sigma_{\rm BH}}{d\Omega_+ d\Omega_- dE_+ dE_-} = \frac{\alpha^3 M}{4\pi^2}\frac{E_+E_-}{p_+\cdot P_i + p_-\cdot P_i - p_+\cdot p_-} S(\kappa)\lambda_{11}(\kappa)\,, \quad (2.1)$$

where

$$\lambda_{11}(k) = \frac{-1}{Q_n^4}\mathfrak{F}_1(Q_n^2)\left\{\frac{k\cdot p_+}{k\cdot p_-}+\frac{k\cdot p_+}{k\cdot p_-}+\frac{Q_n^2 p_+\cdot p_-}{k\cdot p_+ k\cdot p_-}\right\} - \frac{1}{2Q_n^2}\mathfrak{F}_2(Q_n^2)\left\{\frac{(p_+\cdot R)^2+(p_-\cdot R)^2}{k\cdot p_+ k\cdot p_-}\right\},$$

and

$$\kappa = \frac{p_+\cdot P_i + p_-\cdot P_i - p_+\cdot p_-}{M - E_+(1-\cos\theta_+) - E_-(1-\cos\theta_-)},$$

$$\mathfrak{F}_1 = \frac{Q_n^2}{M^2}(F_1+\mu F_2)^2 + \frac{R^2}{2M^2}\left(F_1^2 - \frac{\mu^2 Q_n^2}{4M^2}F_2^2\right),$$

$$\mathfrak{F}_2 = \frac{1}{M^2}\left(F_1^2 - \frac{\mu^2 Q_n^2}{4M^2}F_2^2\right),$$

and

$$R = P_i + P_f.$$

The script form factors $\mathfrak{F}_1$ and $\mathfrak{F}_2$ can also be expressed in terms of the charge and magnetic form factors, $G_E(Q_n^2)$ and $G_M(Q_n^2)$:

$$\mathfrak{F}_1 = 2\{G_E^2 + (Q_n^2/4M^2)G_M^2\},$$
$$\mathfrak{F}_2 = (4/R^2)\{G_E^2 - (Q_n^2/4M^2)G_M^2\}.$$

[5] J. D. Bjorken, S. D. Drell, and S. C. Frautschi, Phys. Rev. 112, 1409 (1958); this reference is referred to as BDF.

$\lambda_{11}(k)$ can then be written in the form

$$\lambda_{11}(k) = -[2/(Q_n^4 k\cdot p_- k\cdot p_+)] \times\{G_E^2(S_1+S_2) + (Q_n^2/4M^2)G_M^2(S_1-S_2)\}, \quad (2.2)$$

where

$$S_1 = (k\cdot p_+)^2 + (k\cdot p_-)^2 + Q_n^2(p_+\cdot p_-),$$
$$S_2 = (Q_n^2/R^2)[(p_+\cdot R)^2 + (p_-\cdot R)^2].$$

It is important to note that S_1 and S_2 are approximately equal in magnitude and are opposite in sign. Because of this second-order cancellation (i.e., $S_1+S_2 \approx S_1/100$) care must be taken when numerically evaluating the cross section. A cancellation also occurs in the dot products $k\cdot p_+$ and $k\cdot p_-$ and near symmetry in $p_+\cdot p_-$ and Q_n^2. For example one usually writes $k\cdot p_+$ as

$$k\cdot p_+ = kE_+(1-\cos\theta_+).$$

However, for the small angles θ_+ which are being considered here $\cos\theta_+ \approx 1$ and there is a second-order cancellation. This cancellation can be eliminated by writing $k\cdot p_+$ as

$$k\cdot p_+ = 2kE_+\sin^2(\theta_+/2).$$

One can also show that

$$p_+\cdot p_- = 2E_+E_-[\sin^2(\theta_+/2)\cos^2(\theta_-/2) + \sin^2(\theta_-/2)\cos^2(\theta_+/2) + \tfrac{1}{2}\sin(\theta_+)\sin(\theta_-)\cos\phi],$$

and

$$Q_n^2 = -4\{1-[2E_+\sin^2(\theta_+/2)+2E_-\sin^2(\theta_-/2)]/M\}^{-1} \times\{[E_+\sin(\theta_+/2) - E_-\sin(\theta_-/2)]^2 + 4E_+E_-\sin(\theta_+/2)\sin(\theta_-/2)[\sin^2[\tfrac{1}{4}(\theta_+ + \theta_-)] + \cos(\theta_+/2)\cos(\theta_-/2)\sin^2(\phi/2)]\}.$$

This form of the expression eliminates the second- to third-order cancellations which the other forms of the expressions contain.

In the above formulas the terms proportional to m^2 have been deleted. The BDF calculation retained some m^2 terms while neglecting others.[5] The Drell and Walecka formulas retain all m^2 terms.[3] A comparison was made between the results obtained from the DW formulas and those obtained from the BDF formulas without any m^2 terms, with the BDF m^2 terms, and with a symmetrized form of the BDF m^2 terms. Note that to consistently neglect m^2 terms it is necessary to set p equal to E. It was found that the BDF formulas without any m^2 terms differed from the DW formulas by less than 0.1%. However, if the BDF m^2 terms or the symmetrized BDF m^2 terms were retained in the BDF formulas, then at symmetry the results differed from the DW results by as much as a factor of 2. The results described in this paper were obtained from the BDF formulas, Eqs. (2.1) and (2.2), in which all m^2 terms have been deleted.

BDF also showed that for the symmetric experiment

$$\sigma_{\rm Compton} = Z^2(E/M)^2\tan^4(\theta/2)\sigma_{\rm BH}, \quad (2.3)$$

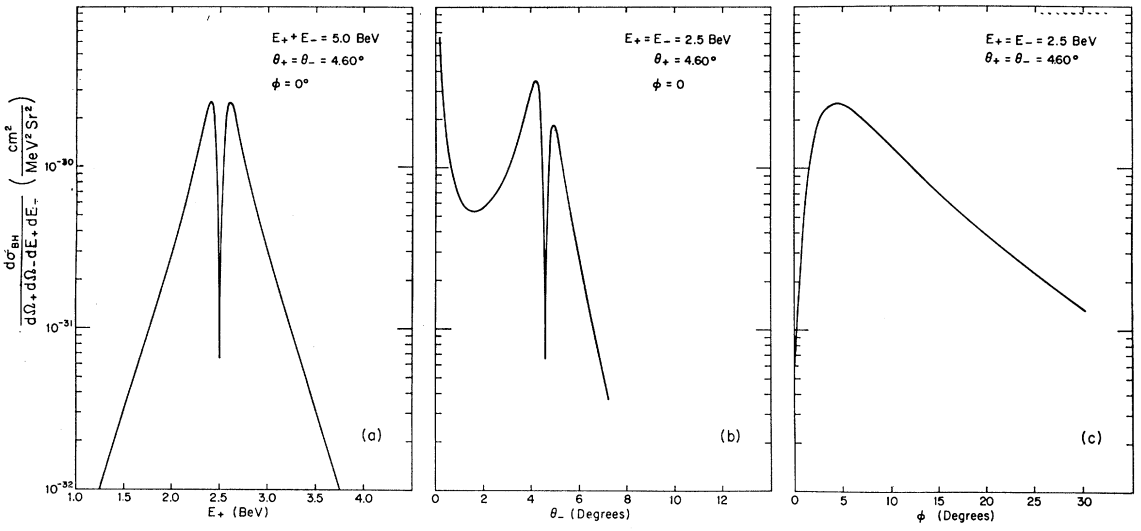

FIG. 4. σ_{BH} as a function of E_+, θ_-, and ϕ.

and that an estimate of the radiative corrections is given by

$$\sigma_{\text{radiative}}=-\frac{2\alpha}{\pi}\ln\left(\frac{2p_+\cdot p_-}{m^2}\right)\left(\ln\frac{E}{\Delta E}-\frac{13}{12}\right)\sigma_{\mathrm{BH}}, \quad (2.4)$$

where[6]

$$\Delta E=k_{\max}-k,$$

and where σ_{BH} is the cross section calculated from only the Bethe-Heitler diagrams [Fig. 1(a)]. The largest angle and energy setting at which electron pairs were observed in this experiment was $\theta=7.46°$, $p=2.25$ BeV/c, $k_{\max}=5.55$ BeV. For this case, $\sigma_{\text{Compton}}/\sigma_{\mathrm{BH}}=4.0\times10^{-3}$, and $\sigma_{\text{radiative}}/\sigma_{\mathrm{BH}}=0.02$.

The above equations are complicated and cumbersome to deal with, especially since the two terms of λ_{11} are opposite in sign and equal in magnitude to several significant figures. In such a situation simple formulas which exhibit the major dependence of the cross section are very useful. One such formula is obtained by considering the symmetric case and by assuming that θ is small. For carbon $\mu=0$ and in this case with

$$\theta\ll1, \quad \phi=0,$$

one finds that

$$\sigma_{\text{sym}}=\frac{d\sigma}{d\Omega^2dE^2}=\frac{\alpha^3}{2\pi^2}\frac{1}{p^3\theta^6}S(k)G_E^2(Q_n^2).$$

This expression is valid only for the symmetric case. The cross section for symmetrical pairs is much smaller than that for slightly asymmetric pairs. Figure 4 shows the cross section σ_{BH} calculated from Eqs. (2.1) and (2.2) with $S(k)=1$/MeV and with the elastic carbon form factors given by[7]

$$G_M=0$$

and

$$G_E=Z\left[1+\frac{\alpha a_0^2Q_n^2}{2(2+3\alpha)}\right]e^{+Q_n^2a_0^2/4}. \quad (2.5)$$

Here $\alpha=\frac{4}{3}$, $a_0=1.635$, and Q_n^2 is expressed in inverse fermis squared. The dip at symmetry is very narrow and deep.

Several approximate expressions for the differential cross section near the dip can be derived. They are:

$$\text{(A)}\quad \theta=\theta_+=\theta_-,\ \phi=0,\ k=E_++E_-=2E,\ \epsilon=E_+-E=E-E_-,$$
$$\sigma=\sigma_{\text{sym}}\left[\frac{1}{1+(2\epsilon/E\theta)^2}\right]^2\left[1+\frac{1}{\theta^2}\left(\frac{2\epsilon}{E\theta}\right)^2\right].$$

$$\text{(B)}\quad E_+=E_-=E=k/2,\ \phi=0,\ \theta_-=\theta,\ \theta_+=\theta+\epsilon,$$
$$\sigma=\sigma_{\text{sym}}\left[\frac{1}{1+(\epsilon/\theta^2)^2}\right]^2\left[1+\frac{1}{\theta^2}\left(\frac{\epsilon}{\theta^2}\right)^2\right].$$

$$\text{(C)}\quad \theta_+=\theta_-=\theta,\ E_+=E_-=E=k/2,$$
$$\sigma=\sigma_{\text{sym}}\left[\frac{1}{1+(\phi/\theta)^2}\right]^2\left[1+\frac{1}{\theta^2}\left(\frac{\phi}{\theta}\right)^2\right]. \quad (2.6)$$

$$\text{(D)}\quad E=\tfrac{1}{2}(E_++E_-),\ e=(E_+-E_-)/(E_++E_-),$$
$$\theta=\tfrac{1}{2}(\theta_++\theta_-),\ a=(\theta_+-\theta_-)/(\theta_++\theta_-),$$
$$\sigma=\sigma_{\text{sym}}\left[\frac{(a+e)^2+\sin^2(\phi/2)+\theta^4/4}{4\{(a+e)^2+\sin^2(\phi/2)+\theta^2/4\}^2}\right],$$
$$\approx\sigma_{\text{sym}}[E^2Q_t^2/4Q_n^4+1],$$

where Q_t is the transverse momentum unbalance.

[6] S. D. Drell (private communication). In the BDF paper Eq. (30) is incorrect. In fact $\Delta E=k_{\max}-k$ and Eq. (29) is valid in the high-resolution limit; that is, when (experimental resolution) $<\Delta E$.

[7] J. H. Fregeau, Phys. Rev. **104**, 225 (1956); R. Hofstadter, Ann. Rev. Nucl. Sci. **7**, 231 (1957).

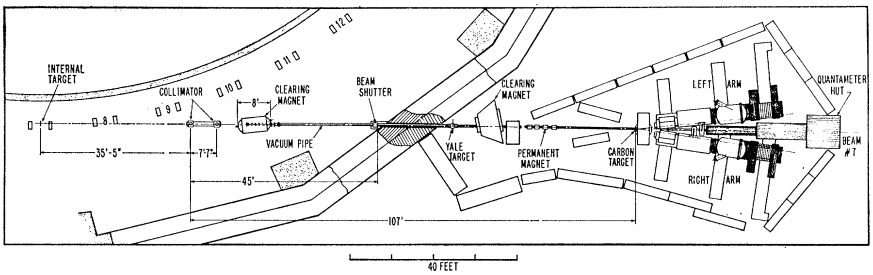

FIG. 5. Drawing showing the general layout of the apparatus and its relationship to the electron synchrotron.

For the symmetric case, approximate expressions for Q_f^2 and Q_n^2 are

$$Q_f^2 \approx -k^2\theta^2/2, \quad Q_n^2 \approx -k^2\theta^4/4. \tag{2.7}$$

Also Q_M^2, the effective mass of the electron-positron final state, is given by

$$Q_M^2 \approx k^2\theta^2.$$

Thus Q_M^2 differs from Q_f^2 by only a factor of 2.

The momentum Q_f of the virtual electron increases as $k\theta$. Thus in an experiment which is to be sensitive to small distance modifications to QED, k and θ should be made as large as possible. However, the symmetric pair-production cross section is proportional to $1/k^3\theta^6$ and is strongly peaked in the forward direction. So in order to probe QED to very small distances it is necessary to measure a very small cross section.

III. APPARATUS

The general characteristics of the apparatus for the wide-angle pair-production (WAPP) experiment were dictated by two main requirements: (1) The system must have a large acceptance since the pair-production cross section is very small, and (2) it must have a very high efficiency for rejecting pions since pion pairs are copiously produced. A magnet-counter system which met these requirements was designed and constructed for this experiment. The system used is shown in Figs. 5, 6, and 7. A large-aperture, axially-focusing magnet, scintillation counters, and a threshold gas Čerenkov counter were used to detect, momentum-analyze, and identify each particle. The two mirror-image systems were mounted on rolling platforms so that various production angles could easily be studied.

At the end of each acceleration cycle (60 cps), the internal electron beam of the CEA was bumped so as to hit a 10-mil-thick tungsten ribbon. The resulting gamma-ray beam pulse was 500 to 600 μsec long and had a 0.8-μsec substructure which corresponded to the orbit filling. The average duty cycle was 1.6%. The gamma-ray beam was collimated by a variable rectangular-aperture collimator which was made of 3.5-in.-thick tungsten alloy blocks. Charged particles were cleared out of the beam by a 30-kG ft magnet. During most of the runs, the apparatus of a Yale-group experiment was located in this beam upstream from the WAPP apparatus. Either a $\frac{3}{4}$-in. carbon target or a 6-in. liquid-hydrogen target was used by the Yale group. Following this target, the beam was cleared by a 50-kG-ft electromagnet and 4-kG-ft of permanent magnets before it impinged upon the WAPP carbon target. At the target, the beam was a $\frac{3}{4}$-in. by 1-in. rectangle. The target was a block of 99.93% pure CCT grade carbon which had a mean density of 1.7 and was supplied by the National Carbon Company. Downstream from the target, the beam was stopped in a quantameter,[8] which was housed in a concrete hut. A thin-wall ion chamber was located just in front of the quantameter inside the hut. From the collimator to the ion chamber, except for two 2-ft air gaps, the gamma beam was in an evacuated aluminum beam pipe.

Charged particles emerging from the target were deflected through an angle of 5.7 deg by a 32-in.-diam circular magnet with a 7-in. gap. This magnet bent the electrons and the positrons away from the gamma-ray beam so that the apparatus could reach smaller production angles. The momentum-analyzing magnet on each arm was a half-quadrupole magnet. This magnet was one-half of a conventional 12-in.-aperture, 48-in.-long quadrupole to which was bolted a 6-in.-thick, 48-in.-long iron plate. The side of this plate is at a magnetic equipotential; thus the plate serves as an image plane and the field in the magnet aperture is the same as that in a conventional quadrupole. The half-quadrupole focused in the vertical plane and was used as a spectrometer by placing a lead obstacle in its center

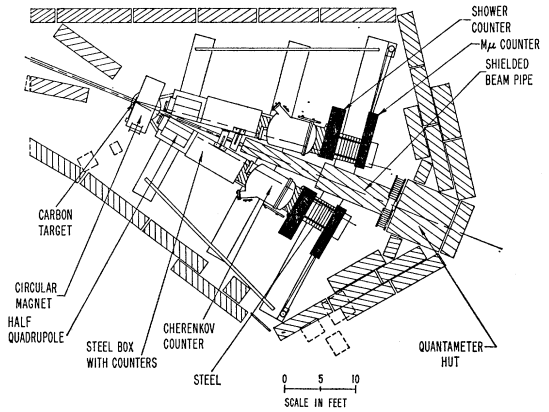

FIG. 6. Top view of the apparatus.

[8] R. R. Wilson, Nucl. Instr. 1, 101 (1957).

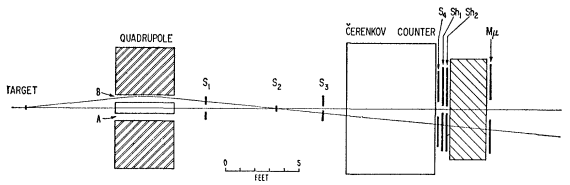

FIG. 7. Schematic drawing of the counter system used to identify and determine the momentum of each particle. A typical particle trajectory is shown in the B channel.

(see Fig. 8). Both the target-to-quadrupole and the quadrupole-to-momentum focus distances were $64\frac{3}{4}$ in. so that the system had unit magnification. The aperture of the magnet was defined by a 3-in.-thick brass mask whose center was about 4 in. from the beam line. This vertical offset determined the minimum production angle which would be attained.

The particle trajectories were defined by several plastic scintillation counters (see Fig. 7). The acceptance of the system was determined by the magnet system and the S_2 counter which was at the focus of each half quadrupole. The $\frac{3}{4}$-in. vertical height of this counter defined the momentum acceptance. The 11-in. length of S_2 accepted all but a few trajectories and determined the width of the particle beam on each arm. Multiple scattering was taken into account by making the S_1, S_3, and S_4 counters oversize. The S_1, S_3, and S_4 counters were $\frac{1}{4}$, $\frac{1}{2}$, and 2 in. oversize in all directions, respectively.

The counters were arranged so as to distinguish those particles which passed through the upper and lower halves of the quadrupoles. Thus there were four channels. Using the notation: L=left, R=right, A=lower half of quadrupole, and B=upper half of quadrupole the four channels were named: LA, LB, RA, and RB. The momentum resolution of each channel was $\pm 4\%$; the solid angle of each channel was 0.8 msr. The angular acceptance was ± 0.6 deg in theta and approximately ± 7 deg in phi.

On each arm a large, threshold-type, gas Čerenkov counter was used to detect electrons and to reject muons and pions. Figure 9 is a section through the central plane of the Čerenkov counter. The index of refraction of the gas was chosen such that 2.75-BeV/c muons would be just below the Čerenkov threshold. Then the Čerenkov angle for high-energy electrons is 2.2 deg and approximately 17 photoelectrons are produced per meter of path if 100% of the light is collected and if the detector has an S-11 response and a 15% quantum efficiency. The gas used in the Čerenkov counter was instrument-grade propane and the normal operating pressure was 10.0 psia. The front window of the counter was made of two layers of 14-mil Mylar.

Most of the details of the Čerenkov counter's optical system were dictated by the very large acceptance which was required. At the entrance to the counter the particle beam was 12 in. high and 18 in. wide. The divergence was 10 deg in the vertical plane and 6 deg in the horizontal plane and the distance from the front window to the light collecting mirror was 80 in. Including the divergence of the light cones, the area from which light had to be collected was 31×31 in. For this purpose a square section from a war surplus 60-in.-diam searchlight mirror with a 25-in. focal length was used. The mirror collected the light and focused it onto a 5-in. 58 AVP photomultiplier which was mounted inside the Čerenkov-counter pressure vessel. To ensure the collection of a large fraction of the light produced, a funnel made of aluminized styrene was mounted in front of the photomultiplier. After extensive optical testing the mirror and photomultiplier positions were adjusted for optimum uniformity of response over the entire entrance area of the counter. Outside of the area actually used the response fell off sharply.

Behind the Čerenkov counters were lead-scintillator sandwiches in which electrons showered. These provided additional discrimination against pions and muons. Each sandwich consisted of: 1 radiation length (rl) of steel, which was the back end of the Čerenkov counter; $\frac{1}{2}$ in. of scintillator, which was also the fourth trigger counter; 2 rl of lead; $\frac{1}{2}$ in. of scintillator; 1 rl of lead; and $\frac{1}{2}$ in. of scintillator. These shower counters were followed by 3 ft of iron and another scintillator which nominally detected only muons.

The smaller trigger counters (S_1, S_2, and S_3) were made from Pilot B scintillator and the large counters were made from Pilot Y scintillator. The S_1 counters were $\frac{1}{4}$ in. thick and the rest were $\frac{1}{2}$ in. thick. Each scintillator was glued to a Lucite light pipe which in turn was glued to the face of an RCA 7850 photomultiplier. The entire assembly was wrapped in aluminum foil and then with black electrical tape. The photomultipliers were electrostatically shielded by the aluminum foil which was at the cathode potential and

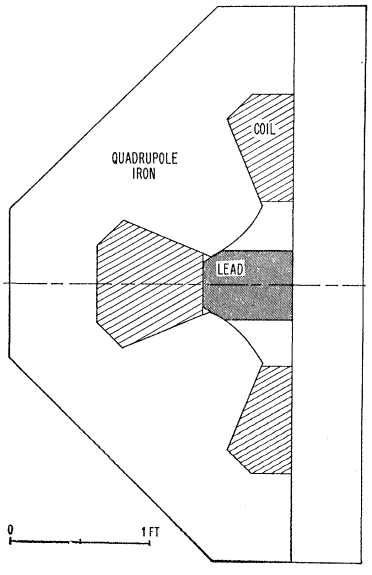

FIG. 8. Half-quadrupole magnet.

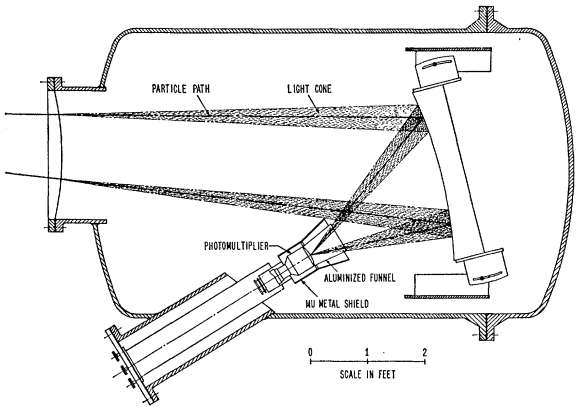

FIG. 9. Threshold gas Čerenkov counter.

magnetically shielded by a commercial mu-metal inner shield and an outer shield of soft iron.

A large amount of lead and steel shielding was placed around the various counters to reduce the singles rates. The S_1, S_2, and S_3 counters were located inside a large steel box which had 6-in.-thick walls between the counters and the beam pipe. Houses with 4- to 8-in.-thick lead walls were built around the S_4-shower arrays and around the muon counters. In addition, above and below the S_2 counters shielding was stacked so as to form a narrow slit which permitted only particles which would count in S_2 to pass. A large fraction of the background was due to spray from the beam pipe and any counter which could view the aluminum beam pipe had a very high singles rate. To the extent possible, lead and high density concrete were stacked between the two arms and the beam pipe to reduce this problem.

The total energy in the gamma-ray beam was measured by CEA quantameter Q1—B. This quantameter exhibited a rather peculiar behavior during the course of the experiment. It was initially filled with a 95% argon, 5% CO_2 gas mixture to a pressure of 780 mm of Hg and sealed off. By the end of the experiment, 5 months later, the pressure had dropped to 684 mm of Hg. In the middle of this period and again at the end, the sensitivity of the quantameter was compared to a freshly filled CEA quantameter and to a quantameter from Cornell.[9] It was found that the sensitivity of the quantameter changed by almost twice as much as the pressure had changed.

The fast electronics used in this experiment were designed and engineered by several members of the experimental group. Each different type of circuit was built in a separate module so that the system would be flexible. The printed circuit boards for the modules were manufactured by a commercial company. The limiter, which was a transistor-driven diode limiter, and the two-stage tunnel-diode discriminator were mounted together on a single module. The fanout was a simple emitter follower circuit. The coincidence circuit was basically the same as one designed by Sugarman for Brookhaven.[10] The dead time of the discriminators was 25 nsec and the fanouts and coincidence circuits had dead times which were less than 1 nsec. As the amplitude of the input pulse to the discriminator varied from threshold to ten times the threshold amplitude, the timing of the output pulse varied by 2 nsec.

The signals from every counter passed through a limiter and into a discriminator. The discriminator outputs were fanned out so that several logical combinations could be formed simultaneously. A fourfold coincidence (13-nsec resolving time) between the scintillation counters $S_1S_2S_3S_4$ defined a charged particle traversing one of the channels. The fourfold coincidences were identified by their channel names. Particles which also had a Čerenkov pulse (abbreviated as C) in fast coincidence were called electrons. A fast coincidence between two particles or two electrons, one on each arm, was called a pair or an electron pair, respectively. These multifold coincidences were named by simply stringing together the names of their constituents. The various rates were scaled by commercial 10-Mc/sec scalers. The scalers were driven by scaler driver circuits triggering on fast-logic pulses. Figure 10 is a skeleton diagram of the left arm, A channel (LA)—right arm, B channel (RB) electronics. The actual logic was much more complicated. Single-channel randoms, pair randoms, and electron-pair randoms were monitored. Furthermore, combinations which included the shower counters and

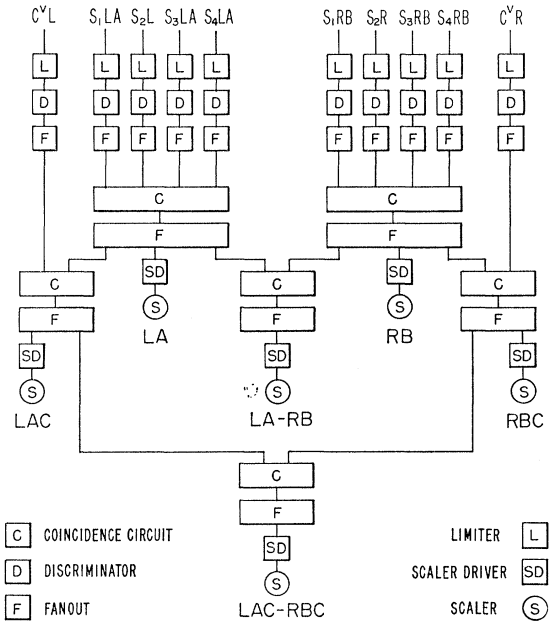

FIG. 10. Simplified LAC-RBC electronics logic block diagram.

[9] R. Fessel and J. R. Rees, Cambridge Electron Accelerator Report No. CEAL-TM-141, 1964 (unpublished).

[10] R. M. Sugerman, IRE Trans. Nucl. Sci. 7, 23 (1960).

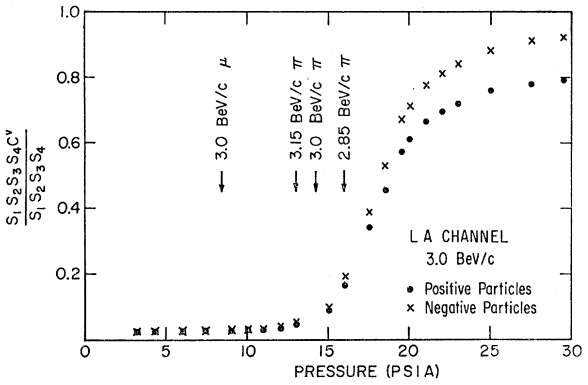

FIG. 11. Čerenkov-counter pressure curve.

mu counters were also formed. An identical set of electronics dealt with the *LB–RA* events.

The ion chamber and quantameter currents were integrated with capacitor-charging-type integrators. These integrators were transistorized versions of a circuit designed by Lewis[11] and modified by Gottschalk. They depended for their precision on the stability of only one capacitor and a 100-V power supply. They had an accuracy of better than 1%. The unit of charge which added 1 count to a mechanical register was known as the click and for the quantameter 1 click equaled 9.92 μC. The scalers, quantameter integrator, and a clock were started and stopped simultaneously.

A four-beam oscilloscope was used to record the Čerenkov counter, shower counter, and mu-counter photomultiplier pulses and the single-channel coincidence pulses for many of the events. The oscilloscope was built around a Dumont cathode ray tube which had four guns in it. A Tektronix model 517A oscilloscope was modified so that it provided the high voltages and horizontal sweep signals for the four-gun CRT. Cascaded Hewlett-Packard wide-band amplifiers were used for the vertical deflection amplifiers.

The signals from the Čerenkov counters, shower counters, and mu counters were passively divided. One-half of each signal went to the fast electronics and the other half went to one input of a 40-channel linear gate. Whenever a trigger pulse occurred the 40 inputs of the gate were opened for 60 nsec. The 40 channels were divided into four sets of 10 and the linear outputs of each set were fed onto a long delay cable. The different outputs were fed onto the cable at different points, which were 80 nsec apart. The signal at the end of each of the four cables was then fed to one of the traces of the four-beam oscilloscope and each trace showed as many as ten signals separated by 80-nsec intervals. A Beattie-Coleman camera, from which the shutter had been removed, was used to photograph the four trace events. The film, Kodak Linagraph Pan, was advanced after each event.

[11] I. A. D. Lewis and B. Collinge, Rev. Sci. Instr. 24, 1113 (1953).

IV. EXPERIMENTAL CHECKS AND PROCEDURE

After the initial runs during which the various counters were timed and voltage plateaued and all other parameters were properly adjusted, about one-half of the running time was spent taking data. The remaining time was spent in studying the characteristics of the apparatus. A large variety of tests were run to ascertain the efficiency, solid angle, reproducibility, and limitations of the apparatus. Since the pair-production rates were low, many of these tests were made on only the single-channel rates at the minimum production angle. To the extent possible these tests were made when the Yale group was the primary accelerator user, controlling the machine energy and other parameters.

4.1 Čerenkov-Counter Efficiency

A measure of the efficiency of the two Čerenkov counters was obtained by running pressure curves. With the magnet system set for 3.0-BeV/c particles, the pressures were varied from 3 to 30 psia, which is well above pion threshold. Figure 11 shows the ratio of the fivefold coincidence rate LAC to the fourfold coincidence rate LA for both positive and negative particles as a function of pressure for the left Čerenkov counter. For data taking, the Čerenkov counters were filled to 10 psia, at which pressure the Čerenkov angle for electrons is 2.2°. At 24.0 psia the Čerenkov angle of 3.0-BeV/c pions is 2.2° and the ratio was 0.86±0.01 for negative particles and 0.74±0.01 for positive particles. The difference between these two numbers was attributed to protons which have a much higher threshold pressure. These ratios are for raw coincidence rates, with no correction for random coincidences, which contribute differently to the four- and fivefold coincicence rates. From measurements of some of the components of the random rates it was estimated that they contribute a correction of 0.02±0.02 to the ratio. Then a lower limit on the efficiency of the left Čerenkov counter was 0.88±0.02. For the right Čerenkov counter, identical measurements gave a lower limit of 0.88±0.02 for the efficiency. The difference between these numbers and 1.0 could be due to kaons which are below the Čerenkov threshold at 24 psia, or to actual inefficiencies in the Čerenkov counters. From the shape of the pressure curve, it would appear that at least 6 to 8% of the difference is due to inefficiencies. Thus the efficiency of each Čerenkov counter is estimated to be 0.91±0.04.

4.2 Pion Contamination

The Čerenkov counter pressures were set below the pion threshold. However, pions, protons, and other heavy particles will produce knock-on electrons in the scintillation counters and in the front windows of the Čerenkov counters. If these electrons have energies

greater than 15 MeV, and if they enter the Čerenkov counter they will count as electrons. This contamination is directly proportional to the flux of particles which are not electrons and depends on the amount of material they traverse. The proportionality constant has been measured in the following manner. It is assumed that all of the pairs which are not electron pairs are pion pairs or pairs of particles all of which have the same knock-on probabilities. That is, $e\pi$ events (those with an electron e in the left arm and a pion π in the right arm) and πe events do not occur. Such events are actually $\pi\pi$ events (pion pairs) in which one of the pions has produced a knock-on electron. At large angles, where the real electron-pair rate is low, many runs were made with one or the other of the Čerenkov counters disconnected from the electron-pair coincidence circuitry. Thus the e-(any particle) event rate was measured. These rates were corrected for the real ee counting rate and it was found that

$$e\pi \text{ rate}/\pi\pi \text{ rate} = \pi e \text{ rate}/\pi\pi \text{ rate} = (0.773\pm0.068)\times10^{-2}. \quad (4.1)$$

This result agrees with estimates which are based on the amount of scintillator and other material which was in front of the Čerenkov counters. The electron-pair contamination is then given by

$$\frac{ee \text{ contamination rate}}{\pi\pi \text{ rate}} = \left(\frac{e\pi \text{ rate}}{\pi\pi \text{ rate}}\right)\left(\frac{\pi e \text{ rate}}{\pi\pi \text{ rate}}\right) = (5.98\pm0.74)\times10^{-5}. \quad (4.2)$$

4.3 Mu Counters

Three feet of steel will completely stop an electron shower, and heavier particles with less than 1.2 BeV of energy will be stopped due to ionization loss. It was hoped that most high-energy pions would be absorbed in nuclear interactions and only high-energy muons would traverse the three radiation lengths of lead of the shower array and the three feet of steel and would count in the mu counter at the end of each arm. Contamination measurements, similar to those made for electrons, showed that for 2.0-BeV/c particles

$$\pi\mu \text{ rate}/\pi\pi \text{ rate} = 0.07.$$

This ratio is somewhat larger than had been expected, and consequently, the pion contamination of the muon pair yields was very large.

4.4 Solid-Angle Studies

Two studies were made of the solid angle subtended by the system. A counter known as $S_1'RA$, which was approximately one-fourth the size of the regular S_1RA, was mounted directly behind S_1RA in the RA channel. The single-channel and pair rates were measured with $S_1'RA$ replacing S_1RA in the electronics. All of the

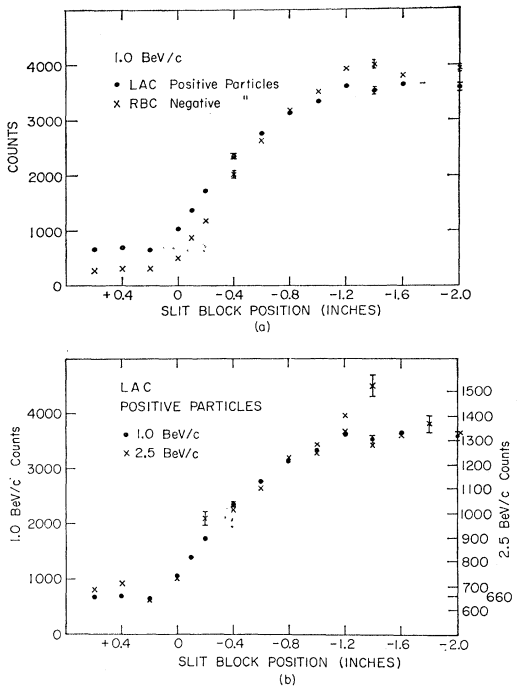

FIG. 12. (a) 1.0-BeV/c horizontal slit curves for the LA and RB channels. (b) 1.0- and 2.5-BeV/c horizontal slit curves for the LA channel.

rates scaled approximately as the ratio of the areas of the two counters.

A set of 1.5-in.-thick tungsten alloy slit blocks was installed in motorized mounts 15 in. in front of the quadrupoles. Each block could be moved from a position in which the quadrupole aperture was completely open to one in which the aperture was completely closed. The single-particle counting rates were measured in all four channels for horizontal and vertical traverses of the blocks. The measurements were made at two different momenta. Figure 12(a) is a plot of the 1.0-BeV/c electron rates in the LA and RB channels for a horizontal traverse. Figure 12(b) is a similar plot for electrons of two different momenta in the LA channel. The slit curves for all four channels were similar in shape and their shape was independent of momentum. This indicates that all four channels had approximately the same solid angle and that the solid angle was independent of momentum. As was expected, 1.5 in. of tungsten did not stop all high-energy pions. The single-particle rates with one slit block closed were one-third of the rates with the slit open. The single-electron rate with one slit block closed was 2 to 3% of the single-particle rate. These electrons were probably produced by the pions in the slit block.

4.5 Chance-Coincidence and Target-Out Rates

There are many different events which can contribute chance coincidences to an eight- or tenfold coincidence

such as was used to measure the pair and electron pair rates. For example, there can be events in which two real particles which pass through nine of the counters are in chance coincidence with a pulse in the tenth counter. Several of these combinations were measured at one point. The only nonzero rate was for random coincidences between real particles in the two arms. This was anticipated since the single-channel rates were high. This random rate was measured for every type of pair coincidence rate measured in data or check runs. In all cases the random rates could be calculated from the coincidence resolving times and the measured single-channel rates.

At many times during the experiment, target out runs were made; on several occasions the apparatus was left on between runs. Not one particle pair was observed during these runs. Nor was an electron pair observed with the slit blocks closed.

4.6 Nonplanar Pairs

The cross section for nonplanar electron pairs is much smaller than that for planar pairs. For most runs only the yields of the approximately planar *LAC–RBC* and *LBC–RAC* electron pairs and *LA–RB* and *LB–RA* pion pairs were measured. However, in a series of runs with $\theta=6.23°$, $p=2.25$ BeV/c, and $k_{\max}=5.5$ BeV the yields of the nonplanar *LAC–RAC*, *LBC–RBC*, *LA–RA*, and *LB–RB* pairs from a $\frac{1}{2}$-in. carbon target were measured. The ratio of nonplanar to planar pairs was 0 to 10.6 ± 1.5 for electrons and 0.060 ± 0.006 for pions. This indicates that at this data point less than 6% of the observed planar-pair yield was due to pairs which were scattered into the apparatus by either multiple scattering in the target or pole face scattering. Calculations indicate that the effect of multiple scattering in the target should be less than a few percent.

4.7 Experimental Procedure

At the beginning of each sequence of runs, a beam picture was taken to check the alignment of the gamma-ray beam. Occasionally small changes in the vertical position of the beam were observed. The beam location varied by $\frac{1}{16}$ to $\frac{1}{8}$ in.; the cause of these changes is not known.

At each data point 50 to 200 electron pairs were detected. This corresponds to a statistical accuracy of 7 to 15%. The running time required to obtain these events varied from 2 to 40 h. Half of the data at each point were taken with the magnets on one polarity and the other half were taken with the magnets on the other polarity. The four-beam scope was triggered to photograph all types of pairs until several thousand pictures had been taken at each data point. For the remainder of the running time it was triggered on only electron and muon pairs.

At the beginning of each data run the magnet settings, counter high voltages, circuit voltages, quantameter voltage, and Čerenkov counter pressures were all checked. The pair coincidence circuits were checked by removing one of the inputs and ascertaining that the resulting rate was identical to the corresponding single-channel rate. The four-beam scope was triggered on the the various single-channel coincidences and all of the individual pulses were visually checked. The carbon-target thickness was chosen to maximize the counting rate and simultaneously to keep the electron-pair chance rate less than 10% and the instantaneous scintillation-counter singles rates below 2 Mc/sec. Generally at high energies a $\frac{1}{2}$-in. target was used and at low energies a $\frac{1}{8}$-in. target. At many of the data points 5- to 10-min runs with a second target thickness were also made so that the dependence on target thickness of the single-channel electron rates could be determined.

During the run the synchrotron parameters which determined the energy and the width of the gamma beam pulses were monitored. The single-particle and single-electron rates were also closely watched for differences between the four channels. Any such difference would have been taken as an indication that something was not functioning properly. The electron pair rates were generally too small to serve as indicators of apparatus failure. The ion chamber was used as a beam monitor when the Yale group was the primary accelerator user. The integrated ion chamber current was frequently compared with the readings of the Yale quantameter current integrator.

A run was ended when enough events had occurred or when 4 h had elapsed. The scaler numbers and the various parameters were then recorded. The scalers had Nixie readouts and they were photographed with a Polaroid camera.

V. DATA ANALYSIS AND RESULTS

5.1 Scaler-Data-Analysis Procedure

During the course of the analysis, several questions arose as to the "correct" procedure for treating the data. The number of events in a single run is a Poisson variable; the square root of the number is the statistical error. For each run, randoms (Poisson variables) must be subtracted, a dead-time correction (Gaussian variable) must be made, and the result normalized to a rate per quantameter click. The several runs made with the same energy and angle parameters should then be combined to obtain a net result. The difficulty lies in the fact that Poisson variables are being combined with Gaussian ones. For Gaussian variables there are a great many theorems which relate how one should propagate errors through a calculation.[12] For Poisson variables the only theorem states that the sum of two Poisson variables is again a Poisson variable. For the mixed case there are no guide rules. One approach

[12] J. Orear, Lawrence Radiation Laboratory Report No. UCRL-8417, 1958 (unpublished).

is to calculate a normalized rate for each run, and to evaluate a weighted mean and chi squared for all of the runs assuming that the result for each run is a Gaussian variable. This assumption is not valid when the event rate is low and there are runs in which there are very few events. In fact there were many runs in which there were no events.

The following procedure was adopted. For runs taken when Yale was the primary accelerator user, the number of quantameter clicks was calculated from the number of ion chamber clicks and the measured ratio of ion chamber to quantameter clicks. For each run and type of event the dead-time correction was applied to the number of quantameter clicks. A correction was also made for the quantameter sensitivity. In all cases the errors were propagated through with the calculations. In analyzing the pair data, the number of corrected quantameter clicks QM was also normalized according to the carbon-target thickness t:

$$\mathrm{QM}_{\mathrm{norm}}=\mathrm{QM}(2.208\ \mathrm{g/cm^2})/t. \tag{5.1}$$

The $\frac{1}{2}$-in. carbon target was 2.208 g/cm^2 thick. In all cases the net combined rate for all runs was then taken to be

$$\text{Net rate}=(E_{\mathrm{tot}}-R_{\mathrm{tot}})/Q_{\mathrm{tot}}, \tag{5.2}$$

where E_{tot} is the total number of events in all runs, R_{tot} is the total number of randoms in all runs, and Q_{tot} is the total number of corrected normalized quantameter clicks in all runs. The error in the net rate was calculated according to the usual error propagation theorems for Gaussian variables[12] with

$$\Delta E_{\mathrm{tot}}=(E_{\mathrm{tot}})^{1/2},$$
$$\Delta R_{\mathrm{tot}}=(R_{\mathrm{tot}})^{1/2}.$$

ΔQ_{tot} is the error in the sum Q_{tot}, and is the square root of the sum of the squares of the errors in the individual $\mathrm{QM}_{\mathrm{norm}}$. Thus the several runs were combined according to Poisson statistics and were treated as one long run. For the pair events this procedure was followed separately for the *LA–RB* events and the *LB–RA* events. The four single-channel rates for each target thickness were treated separately when analyzing the single-particle data. In each case the data taken with the two different magnet polarities were treated independently.

The results which are described below were arrived at by this Poisson-variable procedure. In each case the Gaussian weighted mean and chi squared were also evaluated.[12] The two sets of answers differed by less than one standard deviation and the chi squares had the expected distribution of values except when runs with 0 or 1 events were included. In those cases the two answers differed markedly and the chi squares associated with the Gaussian results were very large.

5.2 Quantameter and Dead-Time Corrections

The peculiar behavior of the quantameter during the course of the experiment was described in Sec. III. There were three points at which the quantameter was compared to other quantameters: In the middle of the experiment when the pressure was at an intermediate value, at the end of the experiment when the pressure was a minimum, and again after it had been refilled with fresh gas. Though the sensitivity changed nearly twice as much as expected for a given change in pressure, the sensitivity was directly proportional to P/T, where P is the pressure and T the temperature. The P/T of the quantameter was measured many times during the experiment. It was an approximately linearly decreasing function of time. A simple function expressing the quantameter sensitivity S as a function of time was derived from the available data. This function was used to correct the number of quantameter clicks for every run. The event rates quoted are in all cases event rates per freshly filled quantameter click. Although the correction was in some cases as large as 20%, since the various factors were all accurately measured the resulting error in the number of quantameter clicks was always less than 1%.

A correction was applied to the data in order to account for losses due to discriminator dead time. Typically for single-channel rates the correction factor was 1.05 and the error in the number of quantameter clicks associated with the correction was 2%. For pair rates the correction factor was generally 1.10 to 1.30 with an error of 0.10. For some runs the correction factor for the electron pair rate was as large as 1.50 with an error of 0.20. The largest contribution to the error in the correction was the error in the duty cycle. The orbit-filling fraction varied from 30 to 70% and it was measured only infrequently.

5.3 Electron-Pair-Data Analysis and Results

For each data point $(\theta,p,k_{\mathrm{max}})$ the above procedure yielded four numbers corresponding to the *LA–RB* and the *LB–RA* events for the two magnet polarities. The weighted mean and the χ^2 of these four numbers was calculated for both the electron pair and the pion pair rates.

For each data point the contamination [see Eq. (4.2)] was subtracted from the mean electron pair rate to yield the net electron pair rate per quantameter click. The contamination correction was never more than 10% of the mean electron pair rate.

The experimental results for the electron pair yield per click for a $\frac{1}{2}$-in. carbon target are summarized in Table II. Some of these results are also shown in Fig. 13. These results include corrections for all known experimental errors except the Čerenkov counter inefficiency. The major factors contributing to the errors quoted are the statistical error and the error associated with the dead-time correction. The latter error dominates at the

TABLE II. Experimental and theoretical electron-pair yields. The angle θ is the angle between each member of the pair and the direction of the incident photon beam; p is the momentum of each member of the pair in BeV/c; k_{max} is the end-point energy of the bremsstrahlung spectrum in BeV; R is the ratio of the experimental yield to the theoretical yield. The experimental yields are the equivalent yields per quantameter click for a $\frac{1}{2}$-in.-thick (2.208 g/cm^2) carbon target. The quantity $\bar{\sigma}_{BH}$ is the electron pair cross section averaged over the apparatus acceptance. The theoretical yields are the yields per quantameter click for a $\frac{1}{2}$-in.-thick carbon target and they include the radiative corrections. The inelastic contributions have not been included in the calculated theoretical yields.

θ (deg)	p (BeV/c)	k_{max} (BeV)	Experimental yield	$\bar{\sigma}_{BH}$ (μb/sr^2 MeV)	$\frac{\sigma_{radiative}}{\sigma_{Bethe\text{-}Heitler}}$	Theoretical yield	R
4.60	0.5	1.25	$(4.40\pm1.03)\times10^{-1}$	1.52×10^{2}	0.018	6.00×10^{-1}	0.73 ± 0.17
		2.5	$(2.18\pm0.13)\times10^{-1}$	1.52×10^{2}	0.103	3.51×10^{-1}	0.62 ± 0.04
	1.0	2.5	$(5.88\pm0.34)\times10^{-2}$	1.88×10^{1}	0.021	7.50×10^{-2}	0.79 ± 0.06
		5.0	$(3.41\pm0.26)\times10^{-2}$	1.88×10^{1}	0.117	4.41×10^{-2}	0.77 ± 0.06
	1.5	5.0	$(1.47\pm0.08)\times10^{-2}$	5.50	0.078	1.73×10^{-2}	0.85 ± 0.04
	2.0	4.5[a]	$(1.21\pm0.13)\times10^{-2}$	2.28	−0.018	9.98×10^{-3}	1.21 ± 0.13
		b	$(1.07\pm0.09)\times10^{-2}$	2.28	−0.018	9.98×10^{-3}	1.07 ± 0.09
		5.0	$(1.05\pm0.04)\times10^{-2}$	2.28	0.023	9.10×10^{-3}	1.16 ± 0.05
		5.15	$(8.57\pm0.93)\times10^{-3}$	2.28	0.032	8.86×10^{-3}	0.97 ± 0.10
	2.25	5.5	$(6.94\pm0.96)\times10^{-3}$	1.60	0.017	6.55×10^{-3}	1.06 ± 0.15
	2.5	6.0	$(7.09\pm0.67)\times10^{-3}$	1.14	0.010	4.72×10^{-3}	1.50 ± 0.14
6.23	1.0	2.5	$(6.83\pm1.56)\times10^{-3}$	2.44	0.022	9.72×10^{-3}	0.70 ± 0.16
		4.0	$(4.13\pm3.24)\times10^{-3}$	2.44	0.010	6.70×10^{-3}	0.62 ± 0.48
		4.5	$(3.40\pm1.47)\times10^{-3}$	2.44	0.112	6.17×10^{-3}	0.55 ± 0.24
		5.0	$(4.92\pm0.72)\times10^{-3}$	2.44	0.123	5.75×10^{-3}	0.86 ± 0.12
	1.5	5.0	$(2.09\pm0.20)\times10^{-3}$	6.97×10^{-1}	0.082	2.20×10^{-3}	0.95 ± 0.09
	2.0	4.5	$(1.29\pm0.19)\times10^{-3}$	2.84×10^{-1}	−0.019	1.24×10^{-3}	1.04 ± 0.15
		5.0	$(1.52\pm0.14)\times10^{-3}$	2.84×10^{-1}	0.024	1.14×10^{-3}	1.34 ± 0.12
		5.5	$(1.43\pm0.32)\times10^{-3}$	2.84×10^{-1}	0.050	1.05×10^{-3}	1.37 ± 0.31
	2.25	5.5	$(1.09\pm0.08)\times10^{-3}$	1.97×10^{-1}	0.017	8.07×10^{-4}	1.35 ± 0.10
	2.5	6.0	$(9.94\pm1.36)\times10^{-4}$	1.39×10^{-1}	0.011	5.76×10^{-4}	1.72 ± 0.24
7.46	1.0	4.0	$(1.94\pm0.41)\times10^{-3}$	6.20×10^{-1}	0.103	1.71×10^{-3}	1.14 ± 0.24
		4.5	$(2.53\pm0.51)\times10^{-3}$	6.20×10^{-1}	0.116	1.57×10^{-3}	1.61 ± 0.33
		5.0	$(1.53\pm0.33)\times10^{-3}$	6.20×10^{-1}	0.126	1.46×10^{-3}	1.04 ± 0.23
		5.5	$(1.37\pm0.35)\times10^{-3}$	6.20×10^{-1}	0.135	1.37×10^{-3}	1.00 ± 0.25
	1.5	5.5	$(6.84\pm2.98)\times10^{-4}$	1.76×10^{-1}	0.098	5.20×10^{-4}	1.32 ± 0.57
	2.25	5.5	$(2.01\pm1.09)\times10^{-4}$	4.83×10^{-2}	0.018	1.97×10^{-4}	1.02 ± 0.55
		5.55	$(3.12\pm0.46)\times10^{-4}$	4.83×10^{-2}	0.021	1.96×10^{-4}	1.59 ± 0.23
10.83	2.0	5.1	$(-0.27\pm1.70)\times10^{-5}$	2.42×10^{-3}	0.033	9.55×10^{-6}	-0.28 ± 1.78
11.70	1.8	5.0	$(-0.07\pm2.08)\times10^{-4}$	1.63×10^{-3}	0.056	5.97×10^{-6}	-1.12 ± 34.88

[a] Target thickness = $\frac{1}{8}$ in. [b] Target thickness = $\frac{1}{2}$ in.

smallest angle where the statistical error is only 5 to 7%. At the larger angles the statistical error is the major contributor to the total error. The points with $\theta=10.83°$ and with $\theta=11.70°$ have net negative yields since fewer electron pairs were observed than were expected due to contamination. At $\theta=10.83$, $p=2.0$ BeV/c, 27 533 pion pairs and only 1 electron pair were observed.

The results presented here are the combined data from many runs. Table III presents the raw data, the various correction factors, and the net electron pair yield [Eq. (5.2)] for the *LAC–RBC* events observed during the several runs taken at four data points for one polarity of the magnet settings. The data runs for the several angles and momenta were not in time sequence. Also the data at any given angle or momentum were not taken during a single unbroken series of runs. In all cases the data were internally consistent and reproducible and there was no indication that the net rates contained systematic errors which depended on time. The relevant chi squares also indicated that the rates were independent of the magnet polarities and that the *LA–RB* and the *LB–RA* apparatus yielded identical results. The point $\theta=4.60°$, $p=2.0$ BeV/c, $k_{max}=5.0$ BeV was used as a reference point and data were taken at this point on four different occasions during the course of the experiment (see Table III).

5.4 Four-Beam-Oscilloscope Film Analysis

Of the 131 000 pictures which were taken with the four-beam oscilloscope, approximately 60% were scanned. The scope traces were projected onto a sheet of graph paper by a small desk top microfilm reader. The scanners were instructed to first check the timing of

TABLE III. Some electron pair data. The number of *LAC–RBC* electron pairs; the number of *LAC–RBC* randoms; the target thickness t, in inches; the number of uncorrected quantameter clicks; the quantameter sensitivity S; the dead-time correction factor $1/\epsilon$; and the number of normalized and corrected quantameter clicks QM_{norm}, are given for all of the runs with one magnet polarity made at four different energy and angle settings.

		LAC–RBC			Uncorrected			
	Run No.	Events	Randoms	t	QM clicks	S	$1/\epsilon$	QM_{norm}
$\theta=4.60°$	15.16	8	1	$\frac{1}{2}$	200	0.90	1.40±0.17	147
$p=1.0+$	15.17	61	1	$\frac{1}{8}$	8000	0.90	1.21±0.09	1728
$k_{max}=5.0$	18.25	2	0	$\frac{1}{8}$	769	0.89	1.18±0.07	174
		71	2					2049
	Net rate $=(3.37\pm0.48)\times10^{-2}$					Contamination $=1.1\%$		
$\theta=4.60°$	12.02	37	0	$\frac{1}{2}$	3700	0.99	1.21±0.08	3102
$p=2.0+$	12.03	35	0	$\frac{1}{2}$	3100	0.99	1.17±0.07	2693
$k_{max}=5.0$	12.04	23	0	1	1391	0.99	1.31±0.13	2076
	12.06	25	0	1	1800	0.98	1.31±0.13	2684
	12.24	17	0	$\frac{1}{2}$	3000	0.98	1.13±0.05	2696
	12.25	1	0	$\frac{1}{4}$	1454	0.98	1.21±0.08	600
	14.03	31	0	$\frac{1}{2}$	2000	0.90	1.51±0.21	1471
	14.05	36	0	$\frac{1}{2}$	4000	0.90	1.51±0.21	2945
	18.34	0	0	$\frac{1}{8}$	769	0.89	1.08±0.03	197
	29.09	5	0	$\frac{1}{2}$	682	0.81	1.10±0.04	761
	29.10	31	0	$\frac{1}{2}$	2600	0.81	1.08±0.03	2953
	29.13	17	1	$\frac{1}{2}$	1400	0.81	1.07±0.03	1602
		258	1					2.378×10^4
	Net rate $=(1.08\pm0.07)\times10^{-2}$					Contamination $=1.4\%$		
$\theta=4.60°$	30.51	4	0	$\frac{1}{4}$	2032	0.81	1.34±0.14	922
$p=2.5+$	30.52	21	0	$\frac{1}{4}$	4584	0.81	1.34±0.14	2082
$k_{max}=6.0$	30.54	12	0	$\frac{1}{4}$	4272	0.81	1.29±0.12	2013
		37	0					5017
	Net rate $=(7.38\pm1.31)\times10^{-3}$					Contamination $=3.8\%$		
$\theta=7.46°$	21.11	0	0	$\frac{1}{4}$	1002	0.88	1.20±0.08	466
$p=2.25+$	21.12	6	0	$\frac{1}{2}$	14401	0.88	1.26±0.10	13016
$k_{max}=5.55$	21.13	4	0	$\frac{1}{2}$	8400	0.88	1.28±0.11	7422
	21.22	0	0	$\frac{1}{2}$	1500	0.88	1.34±0.14	1269
	21.23	2	0	$\frac{1}{2}$	4298	0.88	1.26±0.10	3883
	21.24	4	1	$\frac{1}{2}$	11300	0.88	1.24±0.10	10353
		16	1					3.64×10^4
	Net rate $=(4.12\pm1.15)\times10^{-4}$					Contamination $=9.4\%$		

all pulses. Only those which occurred at the correct time on the trace were accepted. The pulse heights of all acceptable pulses were then measured, recorded, and punched into IBM cards. A package of computer programs was written which sorted the various events, pulse-height-analyzed the different pulses, plotted pulse-height spectra, etc.

The pictures contained a wealth of information about each event. The pulses from the Čerenkov counters, shower counters, and mu counters were all present. The greatest difficulty in dealing with this information was the lack of a calibration. The system was never tested in a beam of pure electrons or pions because such beams were not available. It was necessary to have a basis for deciding which events were electron pairs, pion pairs, etc. The Čerenkov counters were used as the main criteria. Depending on the energy, at the minimum angle from $\frac{1}{2}$ to $\frac{1}{10}$ of the events were electron pairs. At larger angles and at high energies, less than 1/100 of the events were electron pairs. Pictures taken at the small angle which had two Čerenkov pulses were called electron pair events and those taken at large angles which had no Čerenkov pulses were called pion pair events (see Fig. 14). A picture with two mu counter pulses was called a muon pair. The pulse-height distributions in the various counters for each type of event were carefully studied. Initially it was noted that the film data showed a much higher contamination than did the scalers. This was due to the fact that the gates which fed the pulses to the four-beam scope were 60 nsec wide and the Čerenkov counters had very high singles rates, so that the probability of one of the Čerenkov

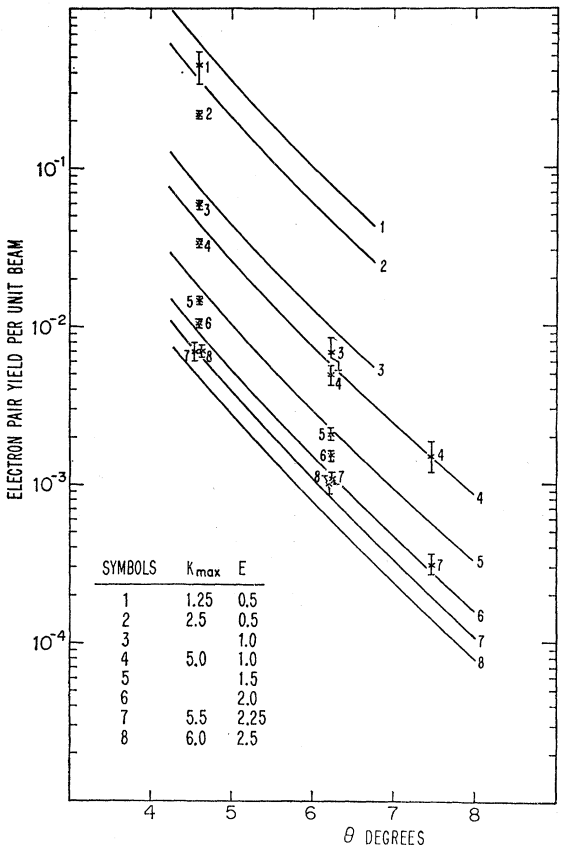

FIG. 13. Experimental and theoretical electron pair yields per unit beam. The solid curves are the theoretical yields calculated by the Monte Carlo integration. The vertical bars on the experimental points are standard deviations.

counters having a pulse within the 60-nsec gate was appreciable. In the last series of runs the output of the fast-logic (13 nsec) coincidences with the Čerenkov counters were also displayed on the four-beam scope. Then the presence of these fast trigger pulses was also required before an event was called an electron pair. Using only the Čerenkov counter information the apparent contamination of the film and the scaler data were then the same.

Since the camera system had a relatively long dead time ($\frac{1}{2}$ sec) not every event which triggered the system was photographed. Not all pictures were scannable because on occasion traces of different events overlapped and could not be separated visually. Sometimes the film was fogged or the camera failed. When the number of electron pairs observed on the film was scaled by the ratio (number of triggers)/(number of events scanned), the result agreed with the scaler data to within the statistical error. For those runs in which every trigger led to a scannable picture the number of electron pairs on the film agreed exactly with the number on the scalers.

Most knock-on electrons and secondary electrons are low-energy electrons which should be distinguishable from high-energy electrons in the shower counters. The shower-counter pulse-height distributions were studied with the intention of using them to further reduce the contamination. The pulse-height spectra of any individual shower counter for either pions or electrons had broad and undistinguished shapes. This is to be expected due to shower fluctuations and the high probability that a pion will produce a low-energy electron somewhere in the shower array. The cleanest spectra and the greatest difference between electrons and pions were obtained by summing for each event the pulse heights in all three of the counters in each counter array. The pulse-height spectra as plotted by the computer for the sum of the three counters S_4LA, Sh_1LA, and Sh_2LA in the LA channel for pions and 2.0-BeV/c electrons are presented in Figs. 15(a) and 15(b), respectively. The same two spectra are plotted in integral form in Fig. 16. By making a cutoff at the appropriate point any desired pion inefficiency can be attained, but at the expense of a corresponding inefficiency for electrons. It was decided to use the point at which the shower array was 95% efficient for electrons as the dividing line between those events which would be called electrons and those which would be called pions. With this criteria the four arrays had the following efficiencies for pions:

Array	Pion efficiency for 95% efficiency for electrons
LA	0.165
LB	0.228
RA	0.325
RB	0.385

Combining this, one finds that the shower arrays are 90.2% efficient for electron pairs and are 6.35% efficient for *LA–RB* pion pairs and 7.41% efficient for *LB–RA* pion pairs. Together with the Čerenkov counters the system is then 90.2% efficient for electron pairs and has an efficiency of 3.8×10^{-6} for *LA–RB* pion pairs and of 4.4×10^{-6} for *LB–RA* pion pairs.

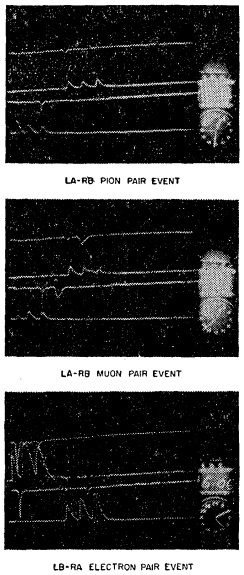

FIG. 14. Sample four-beam oscilloscope film pictures.

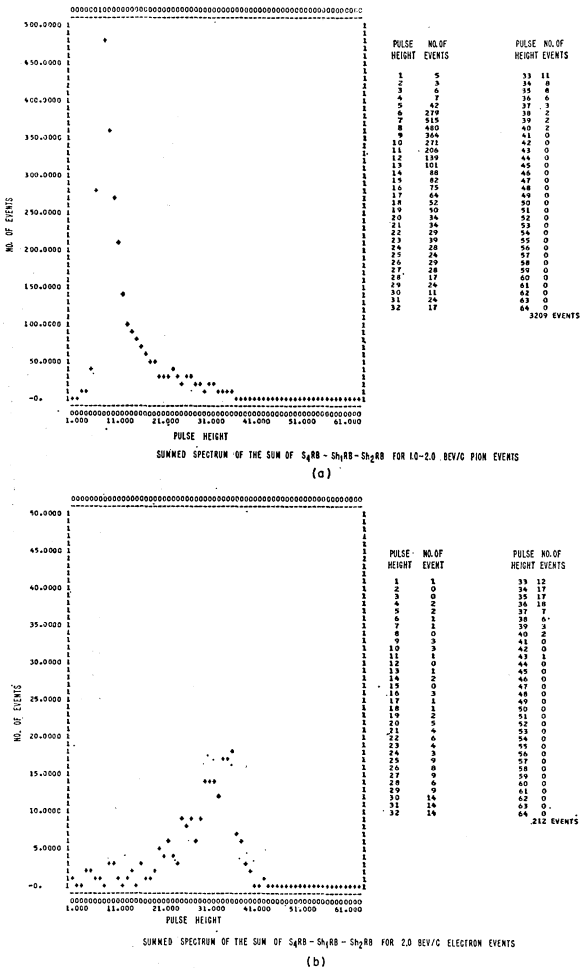

FIG. 15. (a) Summed shower-counter spectrum for 1.0–2.0 BeV/c pions in the LA channel. (b) Summed shower-counter spectrum for 2.0-BeV/c electrons in the LA channel.

The film data for two of the data points were then reanalyzed using both the Čerenkov and shower-counter-information. The net electron pair rates as determined from the film data were found to be identical with the contamination-subtracted scaler rates. The percentage of events rejected by the shower-array criteria was the same as the scaler contamination subtraction to within the statistical error.

For example, at the $k_{\max}=5.5$, $p=2.25$, $\theta=6.23°$ point 164 events were observed to have two Čerenkov pulses on the film. Of these events 146 satisfied the shower-counter criteria for electrons. When the shower-counter efficiency for electron pairs is taken into account, of the 164 events with two Čerenkov pulses 161.8 were actually electron pairs. This indicates that the contamination was 1.3%. However, most of this film was taken before the fast-electron coincidence pulses were also being photographed. Consider now only the 65 pairs with two Čerenkov pulses which were photographed after the fast-electron triggers were being included. The 57 pairs which satisfied the shower criteria did have two fast-electron trigger pulses in their pictures. When the shower-counter efficiency for electron pairs is taken into account, of these 65 pairs, 63.2 were electron pairs. Thus one would expect of the 8 pairs which did not satisfy the shower criteria, 6.3 would be electron pairs and have two fast-electron pulses. Of the 8 pairs, 5 did have two fast-electron pulses. For this data point the scalers gave a total of 74 270 net pion pairs and 243 net electron pairs. Using Eq. (4.2) the pion pair contamination is 4.4 events or 1.8% of the electron pair rate. The film and scaler measures of contamination thus agreed to within the statistical error.

5.5 Single-Channel Data Analysis and Results

For each data point and target thickness the analysis also yielded, after a pion contamination subtraction, eight net single-electron rates and eight net heavy-particle rates corresponding to the four channels and the two magnet polarities. The heavy-particle rates were obtained by subtracting the net electron rates from the measured single-particle rates. The heavy particles were assumed to be mainly pions and protons. The single-electron rates measured at 7.46° and at the larger angles are not meaningful due to the very large contamination subtractions. The high-energy points taken at 6.23° already show significant signs of contamination.

Although, the rates for the two channels on each arm agreed and were independent of magnet polarities, the results for the left and right arms differed markedly.

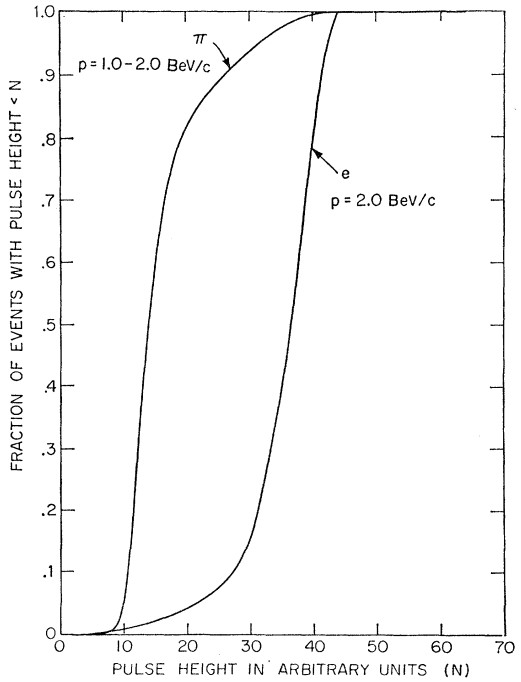

FIG. 16. Integral shower counter-spectrum for pions and electrons in the LA channel.

TABLE IV. The experimental single-arm electron, positron, and heavy-particle yields. The angle θ is the average angle between the particle and the incident gamma-ray beam; p is the momentum of the particle in BeV/c; k_{max} is the end-point energy of the bremsstrahlung spectrum in BeV; t is the thickness of the carbon target in inches. The yields are those for one quantameter click.

θ (deg)	p (BeV/c)	k_{max} (BeV)	t (in.)	Electrons		Positive heavy particles		Negative heavy particles	
				Left arm	Right arm	Left arm	Right arm	Left arm	Right arm
4.60	0.5	2.5	$\frac{1}{4}$	205.63±1.28	248.50±1.73	43.4±2.6	48.9±3.5	38.7±2.9	44.4±3.5
			$\frac{1}{2}$	612.49±5.11	770.73±7.84	112.2±9.4	119.5±17.6	105.8±12.9	102.8±13.3
	1.0	2.5	$\frac{1}{4}$	33.37±0.32	39.40±0.40	88.9±1.3	122.4±1.7	43.3±0.9	48.5±1.1
			$\frac{1}{2}$	96.45±0.73	115.90±1.07	184.6±2.9	251.2±4.0	91.1±2.2	102.3±2.7
		5.0	0	1.53±0.03	0.58±0.02	1.2±0.1	1.2±0.1	0.7±0.1	0.7±0.1
			$\frac{1}{8}$	11.51±0.23	11.62±0.33	48.5±1.4	60.2±2.2	27.7±1.1	29.4±1.1
			$\frac{1}{2}$	73.58±3.11	85.84±4.90	203.6±13.0	272.6±29.1	129.3±15.7	130.3±12.1
	1.5	5.0	0	0.44±0.01	0.15±0.01	1.0±0.1	1.2±0.1	0.7±0.1	0.7±0.1
			$\frac{1}{8}$	3.54±0.05	3.70±0.07	56.1±0.8	61.7±1.0	35.5±0.6	37.8±0.6
			$\frac{1}{2}$	20.88±0.24	25.34±0.35	215.5±2.5	253.1±4.2	139.8±2.2	152.0±2.0
	2.0	4.5	$\frac{1}{8}$	1.72±0.03	1.67±0.03	57.5±0.7	63.3±1.0	40.2±0.6	43.8±0.6
			$\frac{1}{2}$	9.59±0.16	11.08±0.23	235.2±5.0	260.4±3.9	164.7±2.3	182.3±4.3
		5.0	0	0.27±0.01	0.07±0.01	0.8±0.1	1.0±0.1	0.6±0.1	0.6±0.1
			$\frac{1}{8}$	1.67±0.03	1.69±0.04	55.6±0.5	64.5±1.0	41.8±0.6	42.4±0.4
			$\frac{1}{2}$	8.50±0.11	10.49±0.14	216.1±1.6	257.8±4.2	159.8±2.4	173.0±1.4
6.23	1.0	5.0	$\frac{1}{8}$	3.43±0.11	2.99±0.15	46.3±2.1	54.6±2.2	25.9±1.0	27.7±1.4
			$\frac{1}{2}$	19.74±0.88	24.34±1.45	153.8±8.1	219.4±18.4	105.6±8.8	111.7±7.1
	1.5	5.0	$\frac{1}{8}$	1.06±0.04	1.10±0.05	51.3±0.9	58.1±1.1	31.6±0.6	35.6±0.7
			$\frac{1}{2}$	5.98±0.14	7.13±0.20	241.3±5.0	253.0±5.4	140.8±2.8	163.0±3.7
	2.0	5.0	$\frac{1}{4}$	1.01±0.06	1.30±0.09	111.8±4.7	119.8±4.7	76.9±2.8	84.4±3.9
			$\frac{1}{2}$	2.89±0.15	3.85±0.22	231.4±7.2	264.8±12.3	166.8±7.1	178.6±6.2

The four cases for each arm were combined by calculating a weighted mean.

The eight sets of single-electron rates were also least-square fitted to a second-order polynomial, $C+At+Bt^2$, in the target thickness t, where t is expressed in g/cm^2. If data had been taken at only two target thicknesses it was least-squares fit to the form $At+Bt^2$. Thus at each data point the t and t^2 components of the single-electron rate were extracted for each of the eight cases. The four cases for each arm were combined by calculating a weighted mean.

The single-electron and heavy-particle rates for the several target thicknesses are summarized in Table IV. The t- and t^2-dependent components of the single electron rates are summarized in Tables V and VI. The difference between the several rates for the two arms is much larger than the errors. The several electron rates were independent of the magnet polarities and the two channels on each arm yielded the same results. However, the left-arm rates were systematically lower than the right-arm rates by from 5 to 30%.

VI. CALCULATION OF THE THEORETICAL YIELDS

6.1 Introduction

A comparison between the experimental electron-positron pair yields and theory is not easily made. As described in Sec. II the actual cross section has a very deep and narrow dip for symmetrical pairs. The acceptance of the apparatus was approximately twice the width of the dip in θ and p and several times the width of the dip in ϕ. Thus it was necessary to integrate the theoretical cross section over the acceptance to obtain the theoretical electron pair yields.

The acceptance of the apparatus can be described by the function $A_a(p_+,p_-,\theta_+,\theta_-,\phi_+,\phi_-,x,y,z)$. The three variables x, y, and z describe the source point on the target. The six variables, p_+, p_-, θ_+, θ_-, ϕ_+, ϕ_-, describe the magnitude and direction of the positron and electron momenta. These nine variables describe a real pair of particles in relation to the apparatus. A_a can be evaluated for any apparatus configuration and the subscript a refers to enough parameters, such as magnet settings and arm angles, to describe a particular configuration. This function is defined such that for a given setting of the apparatus the expected theoretical yield Y_{th} or counting rate is given by

$$Y_{th}=Q\int_{\text{all space}} A_a(p_+,p_-,\theta_+,\theta_-,\phi_+,\phi_-,x,y,z) \times\sigma(p_+,p_-,\theta_+,\theta_-,\phi_+,\phi_-,x,y,z) \times\rho(x,y,z)dp_+dp_-d\Omega_+d\Omega_-dxdydz, \quad (6.1)$$

where $\sigma(p_+,p_-,\theta_+,\theta_-,\phi_+,\phi_-,x,y,z)$ is the differential cross section, Q is the number of equivalent quanta per click, and $\rho(x,y,z)$ is the differential target thickness normalized such that

$$N=\int_{\text{all space}} \rho(x,y,z)\,dxdydz,$$

TABLE V. The experimental and theoretical electron and positron yields which are proportional to the target thickness. The angle θ is the average angle between the particle and the incident gamma-ray beam; p is the momentum of the electron in BeV/c; $k_{\max}$ is the end-point energy of the bremsstrahlung spectrum in BeV. The yields are those for a carbon target 1 g/cm² thick and for one quantameter click.

θ (deg)	p (BeV/c)	$k_{\max}$ (BeV)	Experimental yield Left arm	Experimental yield Right arm	Theoretical yield Elastic	Theoretical yield Quasi-elastic	Experiment/Quasi-elastic theory Left arm	Experiment/Quasi-elastic theory Right arm
4.60	0.5	2.5	104.33±3.24	118.07±4.68	121.0	121.2	0.86±0.03	0.97±0.04
	1.0	2.5	18.56±0.66	21.04±0.85	21.10	21.31	0.87±0.03	0.99±0.04
		5.0	12.52±0.74	14.37±1.09	19.18	18.81	0.67±0.04	0.76±0.06
	1.5	5.0	4.56±0.14	4.99±0.17	8.24	7.92	0.58±0.02	0.63±0.02
	2.0	4.5	2.81±0.07	2.44±0.09	3.83	3.69	0.76±0.02	0.66±0.02
		5.0	2.20±0.08	2.42±0.09	4.37	4.14	0.53±0.02	0.58±0.02
6.23	1.0	5.0	5.49±0.31	3.70±0.43	6.25	6.04	0.91±0.05	0.61±0.11
	1.5	5.0	1.71±0.11	1.64±0.12	2.95	2.77	0.62±0.04	0.59±0.04
	2.0	5.0	0.53±0.13	0.67±0.20	1.72	1.58	0.33±0.08	0.42±0.13

where N is the number of nuclei per cm² in the target. A_a is a step function on the nine-dimensional space; the apparatus either accepts ($A_a=1$) a pair of particles having a given ($p_+,p_-,\theta_+,\theta_-,\phi_+,\phi_-,x,y,z$) or it does not accept it ($A_a=0$).

The problem of obtaining numbers to compare with the experimental results consists of two parts: (1) the determination of the various functions A_a, σ, and ρ which enter into the integral and (2) the evaluation of the intergral. To reduce the complexity of the problem it was assumed that the target had a uniform density. The incident photon spectrum $S(k)$, which is a factor in σ, [see Eq. (2.1)] may also depend on x, y, and z. Visual inspection of the gamma-beam x-ray pictures indicated that the beam was uniformly dense over the entire beam spot. It was assumed that $S(k)$ did not depend on x, y, or z. The quantities x, y, and z were then treated as parameters so that the problem was reduced to the evaluation of

$$Y_{th}=NQ\int_{\text{all space}} A_{x,y,z,a}(p_+,p_-,\theta_+,\theta_-,\phi_+,\phi_-) \times\sigma(p_+,p_-,\theta_+,\theta_-,\phi_+,\phi_-)dp_+dp_-d\Omega_+d\Omega_-. \quad (6.2)$$

It is convenient to express Y_{th} in terms of an effective cross section $\bar{\sigma}$ defined by

$$\bar{\sigma}=\frac{\int_{\text{all space}} A_{x,y,z,a}(p_+,p_-,\theta_+,\theta_-,\phi_+,\phi_-)\sigma(p_+,p_-,\theta_+,\theta_-,\phi_+,\phi_-)dp_+dp_-d\Omega_+d\Omega_-}{\int_{\text{all space}} A_{x,y,z,a}(p_+,p_-,\theta_+,\theta_-,\phi_+,\phi_-)dp_+dp_-d\Omega_+d\Omega_-}. \quad (6.3)$$

The normalization integral

$$V=\int_{\text{all space}} A_{x,y,z,a}(p_+,p_-,\theta_+,\theta_-,\phi_+,\phi_-) \times dp_+dp_-d\Omega_+d\Omega_-, \quad (6.4)$$

is the volume in six-dimensional phase space accepted by the apparatus. The expected rate is given by

$$Y_{th}=NQV\bar{\sigma}. \quad (6.5)$$

$\bar{\sigma}$ is thus the effective cross section per target nucleus, per unit of phase space, per equivalent quantum.

6.2 Magnet-System Program

Since the two arms were identical and independent systems, A_a could be written as the product of two single-arm acceptance functions

$$A_a(p_+,p_-,\theta_+,\theta_-,\phi_+,\phi_-) =A_a{}^s(p_+,\theta_+,\phi_+)A_a{}^s(p_-,\theta_-,\phi_-). \quad (6.6)$$

A computer program was written to trace out the phase-space volume within which $A_{x,y,z,a}{}^s(p,\theta,\phi)$ equalled 1. This program, RESO, evaluates A^s by a step-by-step trajectory-tracing procedure. Starting at the point x,y,z, on the target, the path or ray is traced through the magnet-counter system for a particle with momentum p and production angles θ and ϕ. The actual physical dimensions and relative positions of the magnets and counters are used and it is assumed that the half-quadrupoles had a pure quadrupole field. At several points within the magnets, the program checks that the ray is inside of the allowed aperture and it checks that the ray passes through all four of the trigger counters. The ray tracing is done for a grid of points in (p,θ,ϕ) space. The size of the grid can be varied and the limits of the accepted phase-space volume can be determined as accurately as desired.

The actual volume in three-dimensional phase space for which $A^s=1$ is not easily pictured. However, the computer program also evaluates the following three

TABLE VI. The experimental and theoretical electron and positron yields which are proportional to the square of the target thickness. The angle θ is the average angle between the particle and the incident gamma-ray beam; p is the momentum of the electron in BeV/c; $k_{\max}$ is the end-point energy of the bremsstrahlung spectrum in BeV. The yields are those for a carbon target 1 g/cm² thick and for one quantameter click.

θ (deg)	p (BeV/c)	$k_{\max}$ (BeV)	Experimental yield Left arm	Experimental yield Right arm	Theoretical yield Elastic	Theoretical yield Quasi-elastic	Experiment/Quasi-elastic theory Left arm	Experiment/Quasi-elastic theory Right arm
4.60	0.5	2.5	78.68±2.32	104.41±3.48	114.9	116.4	0.68±0.02	0.90±0.03
	1.0	2.5	11.36±0.39	14.23±0.54	15.58	16.54	0.69±0.02	0.86±0.03
		5.0	9.06±0.89	10.99±1.38	11.29	11.98	0.76±0.07	0.92±0.12
	1.5	5.0	2.14±0.09	2.89±0.12	2.75	3.21	0.67±0.03	0.90±0.04
	2.0	4.5	0.69±0.05	1.18±0.07	0.74	1.03	0.66±0.05	1.14±0.07
		5.0	0.70±0.05	1.04±0.05	0.72	1.00	0.70±0.05	1.04±0.05
6.23	1.0	5.0	1.46±0.28	3.31±0.43	2.55	2.88	0.51±0.10	1.15±0.15
	1.5	5.0	0.45±0.06	0.72±0.08	0.43	0.62	0.74±0.10	1.17±0.13
	2.0	5.0	0.36±0.08	0.49±0.12	0.06	0.16	2.29±0.50	3.06±0.75

functions:

$$\bar{A}_a{}^s(p)=\int\int A_{x,y,z,a}{}^s(p,\theta,\phi)\,d\theta\,d\phi,$$

$$\bar{A}_a{}^s(\theta)=\int\int A_{x,y,z,a}{}^s(p,\theta,\phi)\,dp\,d\phi,$$

and

$$\bar{A}_a{}^s(\phi)=\int\int A_{x,y,z,a}{}^s(p,\theta,\phi)\,dp\,d\theta.$$

These three functions describe the momentum and angular acceptance of the system and they are shown in Fig. 17 for the case $\theta=4.60°$, $p=2.0$ BeV/c. The coarseness evident in the graphs and especially in $\bar{A}^s(\theta)$ is due to the finite grid sizes used in the computations. The total acceptance of the system was obtained by evaluating the integral

$$V^s=\int\int\int A_{x,y,z,a}{}^s(p,\theta,\phi)\sin\theta\,dp\,d\theta\,d\phi.$$

The phase-space volume for a single arm as computed by RESO was

$$V^s=\bar{p}\times 0.67\times 10^{-4},\quad x=y=z=0,$$

where $\bar{p}$ is the nominal momentum. V^s was also computed for a grid of points which were not at the center of the target and the effective phase-space volume $\bar{V}^s$ was obtained by integrating over the target

$$\bar{V}^s=\bar{p}\times 0.642\times 10^{-4}.$$

For the pair apparatus the volume V, which appears in Eq. (6.5), is then

$$V=(\bar{V}^s)^2=\bar{p}_+\bar{p}_-\times 0.412\times 10^{-8}. \tag{6.7}$$

This number is estimated to have an error of ±7%.

Similar computations for the magnet system without the 32-in. circular magnet were also performed. The functions $\bar{A}_a{}^s(p)$, $\bar{A}_a{}^s(\theta)$, and $\bar{A}_a{}^s(\phi)$ and V^s were the same in this case. Thus the only effect of the circular magnet was to bend the particles away from the gamma beam.

6.3 Integration Program

The main problem was to evaluate the integral I of σ together with A_a:

$$I=\int_{\text{all space}} A_a{}^s(p_+,\theta_+,\phi_+)A_a{}^s(p_-,\theta_-,\phi_-)$$
$$\times\sigma(p_+,p_-,\theta_+,\theta_-,\phi_+,\phi_-)$$
$$\times\sin\theta_+\sin\theta_-dp_+dp_-d\theta_+d\theta_-d\phi_+d\phi_-.$$

This integral was evaluated by a Monte Carlo technique with an IBM 7094 computer.[13,14] The magnet program, RESO, produced a three-dimensional table which defined the phase-space volume within which $A_a{}^s$ equaled 1. For each set of values of $(p_\pm,\theta_\pm,\phi_\pm)$ a table look-up procedure was used to determine whether or not the set was within the accepted volume of the apparatus.

As discussed in Sec. II the Fig. 1(b) Compton diagram contributions are negligible and the radiative corrections are given by σ_{BH} multiplied by a simple smooth function. Since the inelastic form factors are not known, the integration was done only for σ_{BH} as given in Eqs. (2.1) and (2.2). Thus the effective cross section $\bar{\sigma}$ was assumed to be given by

$$\bar{\sigma}=\bar{\sigma}_{\text{BH}}\left(1+\frac{\sigma_{\text{radiative}}}{\sigma_{\text{BH}}}\right),$$

where $\sigma_{\text{radiative}}/\sigma_{\text{BH}}$ is evaluated with the nominal momenta and angles. The photon spectrum is given by

$$S(k)=f(k,k_{\max})/k.$$

To a very good approximation, over a small range in k

[13] H. Kahn, Rand Corporation Report No. AECU-3259, 1954 (unpublished).

[14] R. B. Blumenthal, thesis, Harvard University, 1965 (unpublished).

the photon spectrum is just proportional to $1/k$ and

$$f(k,k_{\max})\approx f(\bar{k},k_{\max}),$$

where

$$\bar{k}=\bar{E}_+ + \bar{E}_-$$

and $\bar{k}$ is the nominal photon energy. Then $S(k)$ can be written as

$$S(k)\approx(\bar{k}/k)S(\bar{k}).$$

For the purposes of the integration, in Eq. (2.1) $S(k)$ was replaced by $\bar{k}/k$; Eq. (6.5) then becomes

$$Y_{th}=NQVS(\bar{k})\bar{\sigma}. \tag{6.8}$$

The elastic form factors entering into $\sigma_{\rm BH}$ were taken from Eq. (2.5). The 7094 computer program was written in the FORTRAN language. With this program about 40 000 evaluations of the integrand were made per minute. The rapidity of convergence depended on the angle θ. For $\theta=4.60°$ it took 130 000 evaluations to converge to a statistical error of 1% and for $\theta=7.46°$ it took only 80 000 to converge to the same accuracy. The program was used to compute $\bar{\sigma}_{\rm BH}$ to a statistical accuracy of 1.0% or less for all of the points at which data were taken. For some cases, as many as 700 000 evaluations were made and $\bar{\sigma}_{\rm BH}$ was computed to a statistical accuracy of 0.4%. The results are tabulated in Table II. The value of $\sigma_{\rm BH}$ at the point $p=p_+=p_-$, $\theta=\theta_+=\theta_-$, $\phi=2°$, which is on the side of the dip, was used as an estimate of $\bar{\sigma}_{\rm BH}$. The actual values of $\bar{\sigma}_{\rm BH}$ differed from these estimates by less than a factor of 2.

There are possible systematic errors in $\bar{\sigma}_{\rm BH}$ due to approximations made in computing the acceptance function and due to the choice of the formulas of Eq. (2.5) for the form factors. The sensitivity of the results to these assumptions has been investigated. DeStaebler considered the additional contribution of quasi-elastic scattering and he showed that[15,16]

$$G_Q^2=Z^2G_E^2+Z(1-G_E^2)G_E'^2, \tag{6.9}$$

where G_E is the elastic form factor, Eq. (2.5), and

$$G_E'^2=G_{Ep}^2\frac{1-\mu_p^2(Q_n^2/4M^2)}{1-Q_n^2/4M^2}.$$

TABLE VII. Weighted mean laboratory angles in degrees. The statistical error in the computation of these angles is 1/2%.

$\langle\theta\rangle$	$\langle\theta\rangle_4$	$\langle\theta\rangle_\sigma$
4.78	4.62	4.60
6.30	6.24	6.23
7.52	7.47	7.46
10.88	10.85	10.83
11.74	11.71	11.70

[15] H. DeStaebler (private communication).
[16] S. D. Drell and C. L. Schwartz, Phys. Rev. **112**, 568 (1958); K. W. McVoy and L. Van Hove, *ibid.* **125**, 1034 (1962).

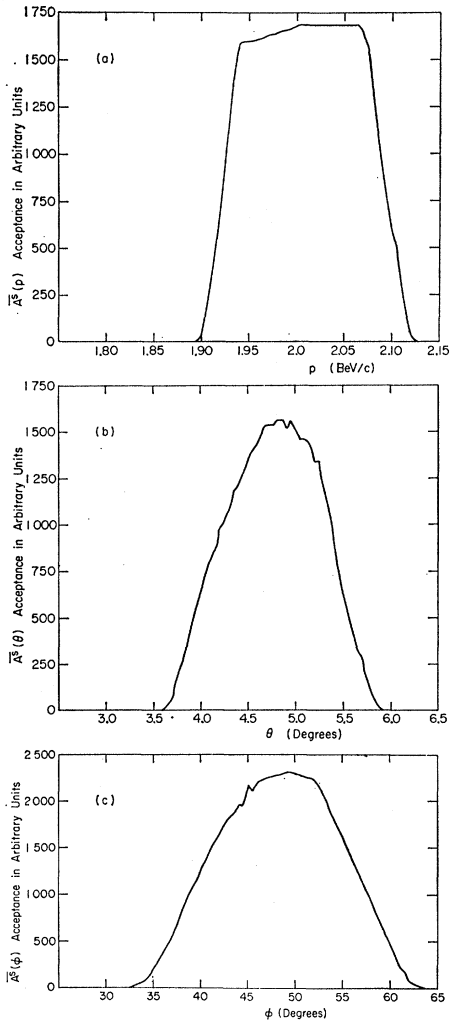

FIG. 17. The acceptance functions $\bar{A}_a{}^s(p)$, $\bar{A}_a{}^s(\theta)$, and $\bar{A}_a{}^s(\phi)$.

Here G_{Ep} and μ_p are the elastic form factor and the magnetic moment of the proton. $\bar{\sigma}_{\rm BH}$ was also evaluated for this form-factor expression. The DeStaebler form factors yielded values of $\bar{\sigma}_{\rm BH}$ which were at most $3.5\pm1.5\%$ higher than those obtained with Eq. (2.5). For $\theta=7.46°$ and $p=2.25$ BeV/c, $\bar{\sigma}_{\rm BH}$ was $18\pm1.5\%$ larger with $G_E=Z$ than with G_E given by Eq. (2.5).

In one version of the integration program the acceptance function was taken to be the product of Gaussians. If the centers of the Gaussians were located at the center of the acceptance (see below) the values obtained for $\bar{\sigma}_{\rm BH}$ agreed with those obtained using the RESO acceptance function to 5%. Also $\bar{\sigma}_{\rm BH}$ was found to be relatively insensitive to 10% changes in the widths of the Gaussians. It is estimated that a systematic error in the acceptance-function calculation can introduce an error of at most $\pm7\%$ in $\bar{\sigma}_{\rm BH}$.

Since parameters such as θ and Q_n^2 varied considerably over the acceptance, a modified version of the integration program was used to evaluate weighted

TABLE VIII. The combined electron pair results and the values of Q_f^2, Q_M^2, and Q_n^2. The entry $[\langle Q_n^2\rangle_\sigma]^{1/2}$ is the average value obtained for the momentum transfer to the nucleus when the momentum transfer is weighted with the electron pair cross section. R is the ratio of the experimental electron pair yield to the theoretical electron pair yield.

θ (deg)	p (BeV/c)	$[-Q_f^2]^{1/2}$ (MeV)	$[Q_M^2]^{1/2}$ (MeV)	$[-Q_n^2]^{1/2}$ (MeV)	$[\langle Q_n^2\rangle_\sigma]^{1/2}$ (MeV)	R
4.60	0.5	57	80	3.2	7.5	0.63±0.04
	1.0	114	160	6.4	15.0	0.78±0.04
	1.5	170	241	9.7	22.5	0.85±0.04
	2.0	227	321	12.9	29.7	1.12±0.04
	2.25	255	361	14.5	33.3	1.06±0.15
	2.5	284	401	16.1	36.8	1.50±0.14
6.23	1.0	154	217	11.8	20.4	0.76±0.09
	1.5	231	326	17.7	30.5	0.95±0.09
	2.0	307	434	23.6	40.4	1.23±0.09
	2.25	346	488	26.6	45.3	1.35±0.10
	2.5	384	543	29.6	50.1	1.72±0.24
7.46	1.0	184	260	16.9	25.1	1.14±0.13
	1.5	276	390	25.4	37.6	1.32±0.57
	2.25	414	584	38.2	55.9	1.50±0.22
10.83	2.0	534	752	71.5	83.7	−0.28±1.78
11.70	1.8	519	730	75.0	85.4	−1.12±34.88

averages of these parameters. If b was such a parameter, the weighted average value of b was computed from

$$\langle b\rangle_\sigma = \int b\sigma A_a \Big/ \int \sigma A_a. \tag{6.10}$$

The mean values of θ, $\langle\theta\rangle$, and the average of θ weighted with a $1/\theta^4$ cross section, $\langle\theta\rangle_4$, were computed by doing a Monte Carlo integration over the acceptance of a single arm. The several corresponding values of θ are summarized in Table VII. In the presentation of the data, the angles θ quoted are the effective mean angles $\langle\theta\rangle_\sigma$. The corresponding values of $\langle p\rangle$, $\langle p\rangle_4$, and $\langle p\rangle_\sigma$ differed by less than $\frac{1}{2}\%$.

The nominal values of Q_f^2, Q_M^2, and Q_n^2 were computed using $\langle\theta\rangle_\sigma$. The weighted averages $\langle Q\rangle^2_\sigma$, of Q_f^2 and Q_M^2 did not differ from their nominal values; however, $[\langle Q_n^2\rangle_\sigma]^{1/2}$ was almost double $[Q_n^2]^{1/2}$ (see Table VIII).

6.4 Theoretical Electron-Pair Yields

The theoretical values of the electron pair yields are given by

$$Y_{th} = NQVS(\bar{k})\bar{\sigma}. \tag{6.11}$$

As described in Sec. 5.1 the experimental data were normalized to a rate per $\frac{1}{2}$-in.-thick carbon target. This target was 2.208 g/cm² thick. Thus

$$N = 1.1085\times10^{23}\ \text{nuclei/cm}^2.$$

The number of photons per click is determined by the quantameter calibration and the size of one click to be

$$Q = 4.70\times10^{13}\ \text{MeV}/k_{\max}.$$

Combining these factors with Eq. (6.7) for V gives for the symmetric case

$$Y_{th} = (\bar{k}/k_{\max})f(\bar{k},k_{\max})\times5.37\times10^{27}\times\bar{\sigma}. \tag{6.12}$$

The function $f(k,k_{\max})$ was calculated by Bethe and Heitler[4,17] and depends upon two functions $f_1(\gamma)$ and $f_2(\gamma)$, where

$$\gamma = 100(m/k_{\max})[v/(1-v)]Z^{-1/3} \quad \text{and} \quad v = k/k_{\max}.$$

The usual approximation made is to assume that $\gamma\approx0$, i.e., complete screening, and that

$$f_1(\gamma) = 4\ln183, \qquad f_2(\gamma) = f_1(0) - \tfrac{2}{3}.$$

A better approximation was made by assuming that

$$f_1(\gamma) = 4\ln183 - 3.64\gamma, \qquad f_2(\gamma) = f_1(0) - \tfrac{2}{3} - 2.59\gamma.$$

Then $f(k,k_{\max})$ is given by

$$f(k,k_{\max}) = [1/\ln(183Z^{-1/3})] \times\{[1+(1-v)^2-\tfrac{2}{3}(1-v)]\ln183Z^{-1/3} + \tfrac{1}{9}(1-v) - 0.91[1+(1-v)^2]\gamma + 0.43(1-v)\gamma\}. \tag{6.13}$$

The values of Y_{th} calculated from Eq. (6.12) for the various data points are given in Table II. These values include the radiative corrections of Eq. (2.4). The radiative corrections as calculated from Eq. (2.4) are listed separately in the table.

6.5 Comparison of the Experimental and Theoretical Yields

The ratios R of the experimental yields to the theoretical yields are given in Table II. The values of R

[17] B. Rossi, *High-Energy Particles* (Prentice-Hall, Inc., Englewood Cliffs, New Jersey, 1956).

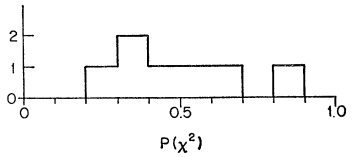

FIG. 18. Frequency distribution of the chi square probabilities obtained when combining the electron pair results for points with different values of $k_{\max}$. $P(\chi_0^2)$ is the integrated probability that χ^2 be larger than the actual value χ_0^2.

obtained at points with different $k_{\max}$ but the same E and θ were equal within the statistical errors. At some points this is true for a very large range in $k_{\max}$. Such data have been combined by calculating a weighted mean and χ^2. The frequency distribution of the χ^2 probabilities is shown in Fig. 18. The combined data are given in Table VIII and are plotted against Q_f^2, Q_M^2, and k^2 in Fig. 19.

6.6 Single-Electron Rates

Simultaneously with the measurements of the electron pair rates, the single-electron rates were measured. The single-electron rates can also be calculated from QED. There are two processes which contribute: (1) pair production in which one particle is produced at a wide angle [Fig. 20(a)] and (2) pair production in the forward direction with the subsequent scattering out of one particle of the pair [Fig. 20(b)]. The yield for process (1) depends linearly on the target thickness t and can be computed by integrating the pair-production cross section over one of the two particles. The yield for process (2) depends on t^2 and the expected rate can be calculated from the total pair-production cross section, the elastic-scattering cross section, and the measured values of the elastic carbon form factor.

Bjorken, Drell, and Frautschi have integrated σ_{BH} over electron variables.[5] It should be noted that their result, Eqs. (8) and (9) in the BDF paper, is not expressed in the laboratory coordinate system, but is in the system in which $\omega=(\omega_0,0)$. In this coordinate system the electron and the recoiling nucleus come out back to back and $p_-\cdot\omega=(\omega^2-M^2)/2$, $E_+=p_+\cdot\omega/\omega_0$, and $E_-=p_-\cdot\omega/\omega_0$. The differential cross section $d\sigma/d\Omega_+dE_+$ was numerically integrated over the bremsstrahlung spectrum, Eq. (6.13). The integration was done for two sets of values of the form-factor parameters a_1, a_2, b_1, and b_2. These corresponded to the elastic, Eq. (2.5), and quasi-elastic, Eq. (6.9), form factors and were:

	a_1	a_2	b_1	b_2
Elastic	5844	2922	3.664×10^6	1.832×10^6
Quasi-elastic	5061	2532	3.091×10^6	1.545×10^6

The resulting theoretical values for the t-dependent component of the single-electron yield are tabulated in Table V. The ratios of the experimental to the theoretical yields with the quasi-elastic form factor are also given in Table V and are shown in Fig. 21(a).

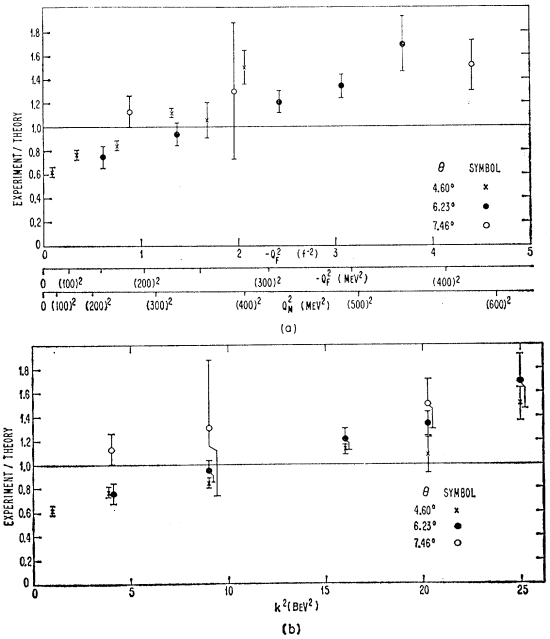

FIG. 19. This figure gives the ratio R of the experimental yields to the calculated yields. Part (a) shows R as a function of the mass of the virtual fermion ($-Q_f^2$) and the mass of the outgoing electron-positron system (Q_M^2). Part (b) shows R as a function of the square of the total energy ($k=E_++E_-$) of the electron-positron pair. The assigned error in the ratio R is due entirely to the errors in the measured yields and contains no estimate of the theoretical uncertainty.

The reliability of the BDF calculation of the t component cross section is uncertain. In their calculation the form factors were expanded in a power series in Q_n^2/M^2 and only the first two terms were kept. This is not a very good representation of the form factor. The accuracy of the t cross section is also in doubt since it is based on the BDF pair cross section which does not treat the m^2 terms consistently.

The differential probability that a photon of energy k produces an electron of energy E at an angle θ by the double process is given by

$$\frac{dP}{d\Omega dE}=\frac{t^2}{2}\frac{d\sigma_{pp}(k,E')}{dE'}\frac{dE'}{dE}\frac{d\sigma_{es}(E',E)}{d\Omega}, \tag{6.14}$$

where σ_{pp} is the pair-production cross section, which is differential only in the energy of the electron, and σ_{es} is

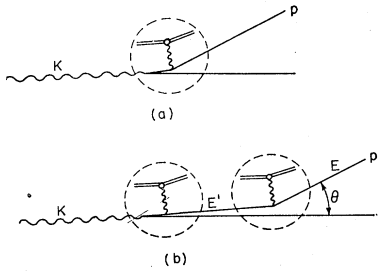

FIG. 20. Feynman diagrams for single-electron production: (a) single process; (b) double process.

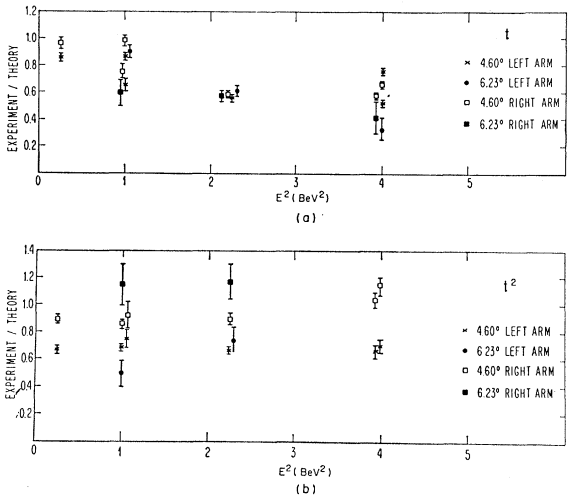

FIG. 21. (a) The ratio of the measured t component of the single-electron yields to the calculated yields as a function of the square of the energy of the electron. (b) The ratio of the measured t^2 component of the single-electron yields to the calculated yields as a function of the square of the energy of the electron.

the cross section for the elastic scattering of an electron of energy E' through an angle θ.

$$E'=\frac{E}{1-(2E/M)\sin^2(\theta/2)},$$

so that

$$\frac{dE'}{dE}=\frac{1}{[1-(2E/M)\sin^2(\theta/2)]^2}.$$

For σ_{es} the Rosenbluth formula with $G_M=0$ was used[18]:

$$\sigma_{es}=\frac{r_0^2}{4(E')^2\sin^4(\theta/2)}\left(\frac{\cos^2(\theta/2)}{1+2(E')^2\sin^2(\theta/2)(E'M)^{-1}}\right)\times\frac{G_E^2(Q_n^2)}{1-(Q_n^2/4M^2)}. \quad (6.15)$$

One can write σ_{pp} as the sum of two terms:

$$\sigma_{pp}=\sigma_n+\sigma_e,$$

where σ_n is the cross section for pair production in the field of the nucleus and σ_e the cross section for pair production in the field of the electrons. σ_e is not negligible; it contributes approximately 18% of σ_{pp}. The expressions for σ_n and σ_e were taken from Wheeler and Lamb.[19]

$$\frac{d\sigma_n}{dE}=\frac{Z^2e^4}{137m^2c^4}\frac{1}{k^3}\{(E^2+E_+^2)(20.75-\tfrac{4}{3}\ln Z)+\tfrac{2}{3}EE_+(20.14-\tfrac{4}{3}\ln Z)\},$$

and

$$\frac{d\sigma_e}{dE}=\frac{Ze^4}{137m^2c^4}\frac{1}{k^3}\{(E^2+E_+^2)[29.1-(8/3)\ln Z]+\tfrac{2}{3}EE_+[28.4-(8/3)\ln Z]\}.$$

In these formulas $E_+=k-E$.

Equation (6.14) was integrated numerically over the photon spectrum. The predicted values of the t^2-dependent component of the single-electron yield are summarized in Table VI for both the elastic and the quasi-elastic form factors. The ratios of the experimental to the theoretical yields are given in Table VI and shown in Fig. 21(b).

There is a large uncertainty in the theoretical single-electron yields, especially in the t^2 component, since the carbon form factor is not known at large values of Q_n^2. Since the energy acceptance of the apparatus was large, the DeStaebler quasi-elastic form factor, Eq. (6.9), is probably a good approximation. Yet it may be in error by as much as 50% at large momentum transfers.

VII. DISCUSSION

7.1 Comparison of the Data with Theory

The results of this experiment for electron pairs are summarized in Tables II and VIII and in Figs. 13 and 19. It is evident that the ratio $R=$(experimental yield)/(theoretical yield) is not 1.0. Two equations which give a least-squares representation of the ratio are

$$R=0.67\{(1.00\pm0.04)-Q_f^2/(313\pm13)^2\}, \quad (7.1)$$

where Q_f^2 is in $(\text{MeV})^2$ and

$$R=0.62\{(1.00\pm0.05)+k^2/(4.31\pm0.17)^2\}, \quad (7.2)$$

where k is in BeV. The χ^2 probability for the first fit is 0.014; the χ^2 probability for the second fit is 0.11. There are two distinct aspects of the disagreement; one is the absolute normalization and the other is the variation of R with energy.

7.2 Normalization of the Data

Since at low energies there are several experiments in which the results are accurately predicted by QED, one expects that in this experiment at low Q_f^2 the ratio R should be 1.0. A deviation of R from 1.0 would indicate that there was either an error in the absolute normalization of the results or a systematic error in the experiment. Some errors which can enter the absolute normalization and an estimate of their magnitude are: synchrotron energy, $\pm\frac{1}{2}\%$; quantameter calibration, $\pm5\%$; calculation of the phase-space volume, $\pm7\%$; evaluation of the $\bar{\sigma}_{BH}$, $\pm7\%$. The extrapolated value of R at $Q_f^2=0$ from the least-squares fit to the data was $R(0)=0.671\pm0.026$. Combining this value with the absolute normalization error estimates gives

$$R(0)=0.67\pm0.08. \quad (7.3)$$

[18] J. W. Motz, Haakon Olsen, and H. W. Koch, Rev. Mod. Phys. **36**, 881 (1964).
[19] J. A. Wheeler and W. E. Lamb, Jr., Phys. Rev. **55**, 858 (1939).

Throughout the analysis it was assumed that the efficiency of the counter system was 1.0. The efficiency of the scintillation counters is not known. A lower limit on the efficiency of each Čerenkov counter is 0.88±0.02, giving a lower limit on the efficiency of the two Čerenkov counter system of 0.78±0.04. An estimate of the efficiency of each counter is 0.91±0.02 (see Sec. 4.1), giving an estimated efficiency of 0.82±0.04 for the detection of electron pairs. $R(0)$ corrected for the Čerenkov counter inefficiency is

$$R_c(0)=0.83\pm0.10. \tag{7.4}$$

7.3 Single-Electron Rates

The greatest deficiency in the experiment was the lack of a calibration of the apparatus with a beam of pure electrons. The many studies of the apparatus consisted mainly of internal consistency tests. The measured single-electron rates when compared to theory provide an independent test of the experimental method. However, it is not clear how significant a test this is because of the large uncertainty in the theoretical yields.

Both the experimental t and t^2 electron yields (see Fig. 21) have approximately the energy and angle dependence predicted by the theories. However, the absolute normalization is in error. The weighted mean of the experiment to theory ratios for left-arm t electrons is: 0.67±0.01; for right-arm t electrons: 0.68±0.01; for left-arm t^2 electrons: 0.68±0.01, and for right-arm t^2 electrons: 0.93±0.02. If these numbers differed from 1.0 because the solid angle was wrong, or because the apparatus was not 100% efficient, the expected normalization for the pair results is just the product of the left- and right-arm normalizations. For the t electrons this product is 0.46±0.01 and for the t^2 electrons it is 0.63±0.02.

One method for correcting for systematic errors in the apparatus is to normalize the pair data to the data for the single rates. That is, if R equals the ratio of experiment to theory, one can form

$$R_n=\frac{R_{\text{electron pairs}}}{R_{\text{left-arm electrons}}R_{\text{right-arm electrons}}}. \tag{7.5}$$

This can be done for both the t and t^2 rates. Figure 22 shows the pair rates normalized in this fashion. This figure shows clearly that there is still a deviation from the theory.

These results suggest either that the apparatus was not 100% efficient or that the acceptance was not as large as calculated. These results also suggest that the acceptances of the two arms were different. For both arms, the energy dependence of the single-electron yields was consistent with the energy dependence of the calculated yields. There are no indications that the excess of wide-angle electron pairs at high energies could be explained by an increase of the apparatus acceptance with energy or scattering of low-momentum electrons from the pole faces of the magnets. This implies that the energy dependence of the electron pair yields is reliable and that only the absolute normalization is in error.

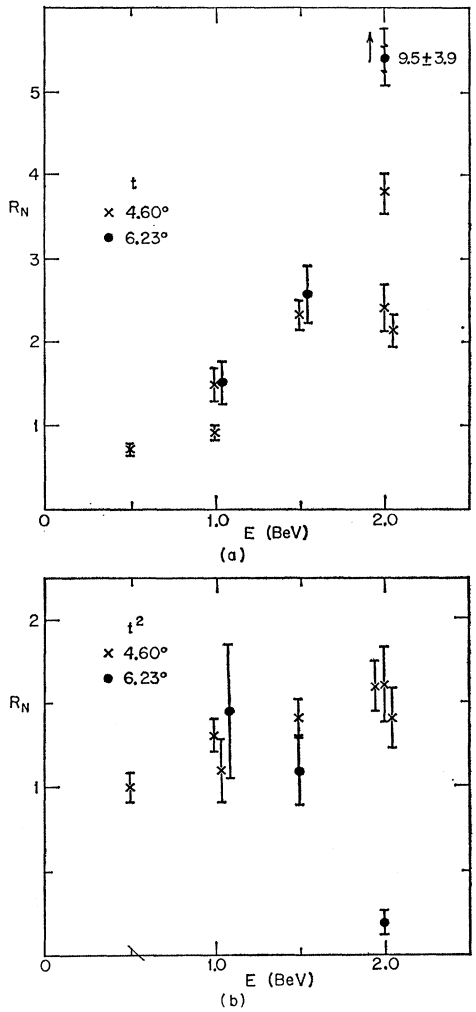

FIG. 22. (a) Electron pair results normalized to the t component of the single-electron yields. (b) Electron pair results normalized to the t^2 component of the single-electron yields.

7.4 Bethe-Heitler Theory

The experimental results were compared with yields calculated from the BDF equations. Carbon does not have a static magnetic moment. It is possible, however, that a magnetic-moment interaction contributes to the cross section in the general inelastic case. The contributions due to inelastic pair production were estimated from the sum rules for inelastic electron scattering[16] and the general formulas of Drell and Walecka.[3] The correction for inelastic processes has roughly the same value at all points, and it becomes significant when the momentum transfer to the nucleus is large enough to reduce significantly the value of the form factor. For those

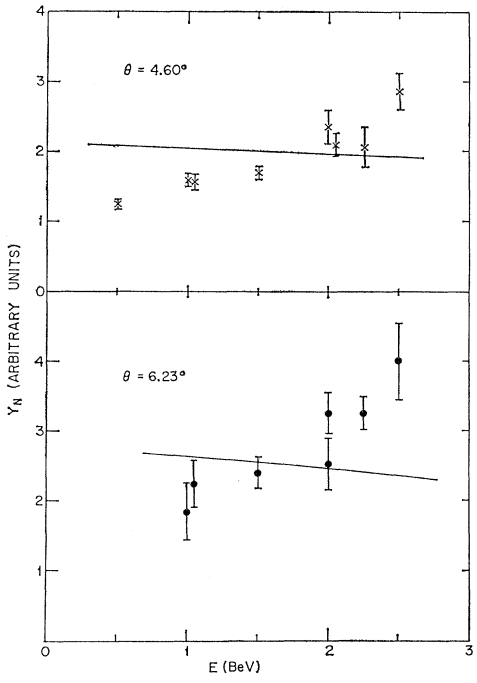

FIG. 23. A plot of the calculated electron pair rates per equivalent quanta without radiative corrections multiplied by E^2 and of the measured rates multiplied by $E^2/(1+\sigma_{\text{radiative}}/\sigma_{\text{BH}})$. [*Note added in proof.* The ordinate should read: E^2Y_N (Arbitrary units).]

points in this experiment at which the momentum transfer to the nucleus was largest, the inelastic contributions increased the theoretical yield by less than 6%. In the integration and analysis inelastic effects were assumed to be negligible and a particular bremsstrahlung spectrum was used. The consistency of the data which differed only in the end point of the bremsstrahlung spectrum, $k_{\max}$ (see Sec. 6.6), implies that these assumptions were correct at least for the low-Q_f^2 points.

One can use a very simple argument to check on the validity of the Monte Carlo integration and to show that at a fixed angle the electron pair rate does not scale properly with energy. Near symmetry the Bethe-Heitler cross section is proportional to $1/E^3$. If it is assumed that at a fixed angle the acceptance of each arm is a function only of $\Delta E/E$, then to a very good approximation the pair yield at fixed angle can be expressed in the form

$$Y_N = Y_{\text{Bethe-Heitler}}/(\text{equivalent quanta}) = \text{const}/E^2. \quad (7.6)$$

Figure 23 shows a plot of the calculated rates without radiative corrections multiplied by E^2 and the measured rates multiplied by $E^2/(1+\sigma_{\text{radiative}}/\sigma_{\text{BH}})$. This figure shows in a manner independent of the details of the Monte Carlo calculation how strikingly the experimental results differ from the theoretical predictions.

7.5 Other Experiments

Most of the tests of QED have been made at low energies. The high-energy experiments have all been pair-production experiments. In an experiment at Stanford in which only one particle of the pair was detected, Richter found agreement between experiment and theory.[20] He found that for $Q_f = 115$ MeV/c, $R = 0.96 \pm 0.14$. Richter's result does not disagree with the results of this experiment.

Alberigi-Quaranta *et al.* measured the photoproduction of muon pairs in carbon and observed no anomalous behavior for momentum transfers Q_f of 135 to 185 MeV.[21]

Recently a high-energy muon pair experiment was performed at the CEA by dePagter *et al.*[22,23] They measured the muon pair-production cross section for several angles but only for a small range in photon energy. In their experiment R was greater than 1.0 but was not a function of Q_f^2. However, the absolute normalization had a large uncertainty. The data points which correspond most closely to those of dePagter *et al.* are

θ	p	R
4.60°	2.0	1.12±0.04
4.60°	2.25	1.06±0.15
6.23°	2.0	1.23±0.09
6.23°	2.25	1.35±0.10
7.46°	2.25	1.50±0.22

For these points R was approximately a constant but it was not 1.0. Thus the results of this experiment are not necessarily inconsistent with those of previous experiments.

7.6 Other Processes

The experimental yields were compared only with the yields expected for the Bethe-Heitler diagrams of Fig. 1 and the Compton diagrams of Fig. 2 whose contribution is negligible. All four of these diagrams are described by QED. There are many processes in which electron pairs may be produced which are not described by QED. For example, at the high energies at which the experiment was performed, other processes may contribute to the Compton effect. Figure 24 depicts two

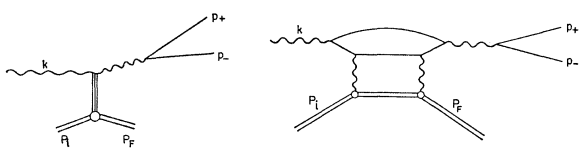

FIG. 24. Diagrams for other Compton processes which can produce electron pairs.

[20] B. Richter, Phys. Rev. Letters **1**, 114 (1958).
[21] A. Alberigi-Quaranta, M. De Pretis, G. Marini, A. Odian, G. Stoppini, and L. Tau, Phys. Rev. Letters **9**, 226 (1962).
[22] J. K. dePagter, A. Boyarski, G. Glass, J. I. Friedman, H. W. Kendall, M. Gettner, J. F. Larrabee, and R. Weinstein, Phys. Rev. Letters **12**, 739 (1964).
[23] G. Glass, thesis, MIT, 1964 (unpublished).

such processes. Several calculations indicate that these diagrams are negligible.[24,25]

Drell has re-examined the question of the contribution of the Compton diagrams and found the correction to be less than 1%.[25] In one calculation Drell used the experimentally observed total photon absorption cross section and the Kramers-Kronig relation for forward scattering of light to estimate the forward Compton scattering. He then estimated the electron-pair cross section by assuming that the outgoing photon makes an electron-positron pair and neglecting the fact that the virtual photon which produces the lepton pair is off the mass shell. At the largest angle and energy observed in the electron pair experiment the correction to the Bethe-Heitler cross section at the symmetry point where the cross section is a minimum was $2\frac{1}{2}\%$. When this correction is averaged over the experimental resolution, the correction is less than 0.2%. In a second calculation Drell used the measured photoproduction cross sections for the rho and an experimental upper limit on the branching ratio for the decay of rhos into electron-positron pairs to estimate the correction due to this process. Again in this case Drell found that when the correction was averaged over the experimental resolution, the net correction was less than 1%. Krass has independently come to a similar conclusion.[24]

It is still a possibility that the electromagnetic decay into an electron-positron pair of some particle was being observed. The electron pair excess, however, does not show a peak at any mass. The principal candidate for this particle was the ρ meson which has a mass of 750 MeV. A run was made at the mass of the ρ meson in order to investigate this possibility. At this mass 27 533 pion pairs[26] and only one electron pair were observed. The calculated yield due to Bethe-Heitler pair production was 1.5 electron pairs, and 1.6 electron pairs were expected because of the contamination. This implies that

$$\frac{\rho \rightarrow e^+ + e^-}{\rho \rightarrow \pi^+ + \pi^-} < 10^{-4} \qquad (7.7)$$

and that the excess of electron pairs was not due to ρ decay.

The difference between the theory and experiment could also be due to the presence of some new particle which is coupled to an electron and a gamma ray.[27] F. E. Low has suggested that the pair anomaly could be explained without contradicting other experiments by postulating a heavy electron which can decay into an ordinary electron and a gamma ray. Experiments performed to detect this particle have so far not revealed its existence.[28] Another possible explanation is the existence of a massive photon which can decay into an electron-positron pair.

VIII. CONCLUSIONS

This experiment is a new test of quantum electrodynamics at high energies and small distances. The experimental results do not agree with the predictions of the theory; they indicate a breakdown of the theory or the presence of other processes.

ACKNOWLEDGMENTS

We would like to thank the staff of the Harvard Cyclotron for their aid in the design, construction, and setting up of the apparatus. We thank the staff of the Cambridge Electron Accelerator for their many services. We gratefully acknowledge the assistance of C. Friedberg, E. Petraske, J. K. Randolph, J. J. Russell, and J. Tenenbaum. We also wish to thank the many scanners, computer programmers, and research assistants who have worked with the WAPP group during the past three years. We wish to thank Professors J. D. Bjorken and S. D. Drell for several illuminating discussions of the theory. We are indebted to the Harvard Computation Center and the U. S. Atomic Energy Commission Computing and Applied Mathematics Center at New York University for making their facilities available to us.

[24] Allan Krass, Phys. Rev. **138**, 1268 (1965).

[25] S. O. Drell, in *Proceedings of the International Symposium on Electron and Photon Interactions at High Energies* (Springer-Verlag, Berlin, 1965), Vol. I, pp. 71–90.

[26] In a subsequent experiment we have shown that at least 90% of these pion pairs come from the decay of rho mesons. L. J. Lanzerotti, R. B. Blumenthal, D. C. Ehn, W. L. Faissler, P. M. Joseph, F. M. Pipkin, J. K. Randolph, J. J. Russell, D. G. Stairs, and J. Tenenbaum, Phys. Rev. Letters **15**, 210 (1965).

[27] F. E. Low, Phys. Rev. Letters **14**, 238 (1965).

[28] C. Betourne, H. Nguyen Ngoc, J. Perez-y-Jorba, and J. Tran Thanh Van, Phys. Letters **17**, 70 (1965); R. Budnitz, J. R. Dunning, Jr., M. Goitein, N. F. Ramsey, J. K. Walker, and Richard Wilson, Phys. Rev. **141**, 1313 (1966); H. J. Behrend, F. W. Brosse, J. Engler, E. Ganssauge, H. Hultschig, S. Galster, G. Hartwig, and H. Schopper, Phys. Rev. Letters **15**, 900 (1965); H. Kendall (private communication).

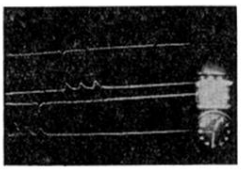

LA-RB PION PAIR EVENT

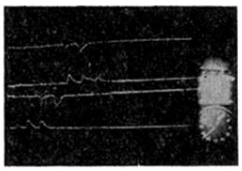

LA-RB MUON PAIR EVENT

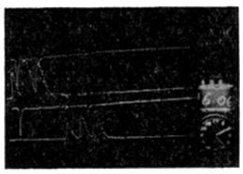

LB-RA ELECTRON PAIR EVENT

FIG. 14. Sample four-beam oscilloscope film pictures.